In Situ Observations of the Microphysical Properties of Wave, Cirrus, and Anvil Clouds. Part I: Wave Clouds

BRAD A. BAKER AND R. PAUL LAWSON

SPEC Inc., Boulder, Colorado

ABSTRACT

The microphysical properties of wave clouds based on data collected during 17 missions flown by a Learjet research aircraft are presented and discussed. This extensive dataset expands upon previous aircraft studies of wave clouds and introduces some new findings. While most aspects of the observations are consistent with basic cloud physics, some aspects remain difficult to interpret. Most notable among these are ice nucleation and aspects of the dynamical structure of wave clouds. A new hypothesis to explain the ice nucleation behavior is presented.

The average and standard deviation of bulk microphysical parameters are presented for various locations within the wave clouds. Using digital imagery from a cloud particle imager (CPI), the shapes of ice particles are studied and crystal habits are classified. For certain categories—rosette shapes, columns, and irregular shapes—power-law parameterizations of particle area from particle length are presented. Polycrystals with rosette shapes dominate the ice mass while small spheroidal and irregularly shaped crystals dominate the ice number concentration.

The concept and difficulties of using wave clouds as natural cloud physics laboratories are discussed and evaluated. A study of the riming threshold size of columns is in good agreement with the results of previous studies, showing that column width is the predominate factor in determining riming threshold. The first reported studies of the riming threshold size of rosette shapes and the threshold size for side-plane growth are presented.

1. Introduction

Mid- and upper-tropospheric ice clouds, including wave, cirrus, and anvil clouds, have become the focus of several recent field studies due to their importance in the earth's radiation budget. Accurate measurements of the size, shape, and concentration of ice particles in these clouds are critical to improving our understanding of the physics of ice formation and the radiative effects clouds have on global climate change. While wave clouds do not cover nearly as much area as cirrus and anvil clouds, they do allow us to make observations to attempt to study the physical processes of all these clouds in a more controlled situation.

In situ microphysical measurements of wave clouds investigated with a Learjet research aircraft over the Front Range of the Colorado Rocky Mountains are

presented. The data are unique in that, for the first time, extensive observations of ice particle size, shape, riming, and side-plane growth were collected using a cloud particle imager (CPI; Lawson et al. 2001). The dataset is also larger than those of previous studies. It is composed of 133 cloud penetrations (i.e., horizontal legs) in 17 wave clouds encompassing a temperature range from $-15°$ to $-60°C$.

The data are discussed in light of basic cloud microphysical processes. Many aspects of the observations are expected and explainable. However, some aspects remain difficult to interpret from our current understanding of cloud microphysics and within the limitations of the dataset. In particular, the lack of vertical velocity and accurate relative humidity measurements is a source of uncertainty in our interpretations. Throughout this presentation of the data, the repeatability of the observations as well as their consistency with the expectation of basic cloud physics will be emphasized. Hypotheses for some of the unexpected observations are also presented.

Corresponding author address: Brad A. Baker, SPEC Inc., Suite 200, 3022 Sterling Circle, Boulder, CO 80301.
E-mail: brad@specinc.com

2. Previous findings

Heymsfield and Miloshevich (1993, hereafter HM93) report findings from earlier jet aircraft investigations of wave clouds over the Colorado Front Range. The HM93 study was limited to five missions and 30 cloud penetrations, of which data from two clouds are presented in their paper. Conclusions from HM93 germane to this research are summarized below.

- Homogeneous nucleation is the primary mechanism responsible for ice formation in the wave clouds studied.
- Virtually no ice was observed in water-saturated cloud regions at temperatures warmer than about $-32°C$.
- There is a common "glaciation transition signature" that is discernable from data collected by the particle probes at the transition from either all-water or mixed-phase to glaciated cloud, that is, a sudden reduction in the number concentration of small (water) particles, accompanied by an increase in the mean particle size and concentration of ice.

Heymsfield and Miloshevich (1995, hereafter HM95) report similar findings as HM93, extending the observations to colder temperatures ($-56°C$). In particular, below $-37°C$, the transition to glaciated cloud is interpreted as homogeneous freezing of solution droplets, too small to be seen with the instrumentation of this current study.

A recent study reported by Field et al. (2001, hereafter F01) was conducted in Scandinavia and utilized more advanced cloud particle instrumentation than HM93 and HM95. The results are based on flights through seven clouds that ranged in temperature from $-12°$ to $-40°C$. The germane conclusions from F01 are as follows.

- Homogeneous nucleation appeared to be dominant at temperatures $<-35°C$.
- Heterogeneous nucleation was occurring in the temperature region from $-15°$ to $-35°C$ and produced ice concentrations from 1 to 10 cm^{-3}.
- Heterogeneous nucleation occurred after the supercooled liquid droplets reached their maximum size.
- Possible candidates for the heterogeneous nucleation process are immersion freezing and contact nucleation.
- Essentially the same glaciation transition cloud signature was as described above from HM93.

The results from F01 are mostly consistent with HM93, except that unlike HM93, F01 found that heterogeneous nucleation was active at temperatures $>-35°C$, whereas HM93 found no evidence of ice at temperatures $>-32°C$. However, the HM93 study was not as extensive as F01, so the limited dataset was likely biased by undersampling. Similarly, the results of our study are to a large extent consistent with F01 but there are notable exceptions. This is again presumably due to the larger dataset used in the current study.

3. Data collection and segregation

The data discussed in this paper were all collected using a Learjet Model 25 research aircraft that was leased and operated by SPEC, Inc. Placement of the sensors on the aircraft is shown in Fig. 1 and a list of the instrumentation used in this study is found in Table 1. Since the Learjet has a ceiling of 45 000 ft MSL, it has the capability of making measurements throughout the vertical extent of midlatitude wave clouds. The sampling airspeed of the Learjet ranged from approximately 150 m s^{-1} at FL250 (25 000 ft or 7.6 km) to 175 m s^{-1} at FL400 (40 000 ft or 12.2 km).[1]

The principles of operation of the forward scattering spectrometer probe (FSSP) and the two-dimensional cloud (2D-C) probe are discussed by Knollenberg (1981). Limitations of the FSSP are discussed by, for example, Cooper (1988), Brenguier (1989), Baumgardner et al. (1990), and Gayet et al. (1996). Laboratory and wind tunnel measurements presented in Strapp et al. (2001) suggest that the time response of the 2D-C limits its minimum detectable particle size to approximately 75 μm at 100 m s^{-1}. Subsequent laboratory and airborne measurements by Lawson et al. (2006a) suggest that the 2D-C probe does not image water drops <100 μm in diameter at 100 m s^{-1} and that approximately 2% of water drops with diameters <150 μm are imaged at that airspeed. The imaging efficiency of the 2D-C is expected to continue to degrade with increasing airspeed (Baumgardner and Korolev 1997). The Nevzorov liquid water content (LWC) and total water content (TWC) probes are discussed by Korolev et al. (1998). In all-ice clouds, the Nevzorov TWC probe measures ice water content (IWC). Recent investigations comparing data from the Nevzorov probe and from counterflow evaporation instruments on a NASA WB-57F research aircraft suggest that the Nevzorov IWC may be underestimated in all-ice clouds. Based on wind tunnel experiments, the Nevzorov underestimate

---

[1] The abbreviation FL is a standard designation used in aviation to designate flight level and refers to pressure altitude in hundreds of feet. Here, FL is used, along with pressure altitude in feet, because these units were used in the analysis of the data. The corresponding Système Internationale (SI) units are also given in parenthesis.

FIG. 1. Photograph of the Learjet showing placement of sensors used in this research. See Table 1 for details on the sensors.

is suspected to be the result of some of the ice particles bouncing out of the heated cone (A. Korolev 2004, personal communication). The Rosemount Icing Probe is described in Mazin et al. (2001) and Cober et al. (2001). Unlike the cryogenic dewpoint hygrometer used by HM93, the device used here (Buck Research Model CR-1A) was found not to have adequate response for use in determining supersaturation with respect to ice and therefore has not been used in this study. We did not determine whether the inadequate response characteristics of the cryogenic hygrometer were a fundamental problem with the device or a result of our installation on the Learjet. Horizontal winds were computed using GPS position and heading from the Learjet

avionics instrument. When in straight flight, the Learjet winds were in general agreement with reports from other commercial airliners in the area. Unfortunately, there was no instrumentation for computing vertical winds. Based on pilot observations of aircraft response, however, it was found that the vertical winds in all of the wave clouds encountered were very light, estimated to be less than ± 2 m s^{-1}.

The basic Learjet flight profile was to fly along the horizontal wind direction, which is usually nearly orthogonal to the ridgeline that is forming the waves, alternating upwind and downwind level penetrations, at multiple altitudes, through the depth of the cloud. None of the wave clouds exceeded the 45 000 ft MSL service

TABLE 1. Specifications for sensors installed on the Learjet and used for the wave cloud research.

Equipment list	Sensor manufacturer and model No.	Range	Accuracy
Temperature	Rosemount model 102 and 510-BH amp	$-50°$ to $+50°$C	0.5°C
Dewpoint	Buck Research CR-1A	$-10°$ to $+50$	N/A
Altitude	Rosemount 1201	0–1013 mb	1 mb
Air speed	Rosemount 1221	0–220 m s^{-1}	1 m s^{-1}
Aircraft position	Garmen model GPS-92	N/A	50 m
Aircraft heading	Learjet Sperry directional gyro	0°–360°	1°
Horizontal wind	GPS plus heading information	0°–360°, 5–100 m s^{-1}	5°, 5 m s^{-1}
2D-C	PMS model OAP-2D-C	33–1056 μm	N/A
FSSP	PMS model FSSP-100	3–45 μm	N/A
CPI	SPEC model 230-X	10–2000 μm	N/A
Cloud liquid water	Sky Tech Nevzorov LWC probe	0–4 g m^{-3}	N/A
Cloud total water	Sky Tech Nevzorov TWC probe	0–10 g m^{-3}	N/A

TABLE 2. Cloud-base and cloud-top altitude, temperature, and duration in cloud for wave clouds investigated by the SPEC Learjet and presented in this study.

Date	Cloud-base and -top temperatures (°C)	Cloud base (ft × 100)	Cloud top (ft × 100)	Duration in cloud (h)	Number of legs	Type of wave cloud
28 Mar 00	−21 to −28*	FL 210 (6.4 km)	FL 235 (7.2 km)	1.3	7	Multiphase
26 Apr 00	−25 to −31*	FL 240 (7.3 km)	FL 260 (7.9 km)	1.0	8	Multiphase
28 Nov 00	−43 to −48	FL 295 (9.0 km)	FL 310 (9.5 km)	0.8	5	All ice
5 Dec 00	−17 to −36	FL 160 (4.9 km)	FL 260 (7.9 km)	1.0	8	Multiphase
7 Dec 00	−29 to −51	FL 250 (7.6 km)	FL 330 (10.0 km)	1.5	11	Multiphase
16 May 01	−24 to −40	FL 240 (7.3 km)	FL 310 (9.5 km)	1.5	8	Multiphase
20 Oct 01	−27 to −60	FL 250 (7.6 km)	FL 390 (12.0 km)	2.0	10	Multiphase
11 Oct 02	−17 to −34	FL 210 (6.4 km)	FL 280 (8.5 km)	1.0	9	Multiphase
7 Nov 02	−40 to −59	FL 300 (9.0 km)	FL 375 (11.4 km)	2.0	10	All ice
8 Nov 02	−26 to −38	FL 230 (7.0 km)	FL 270 (8.2 km)	1.0	4	Multiphase
12 Nov 02	−20 to −36	FL 200 (6.0 km)	FL 270 (8.2 km)	1.3	11	Multiphase
18 Nov 02	−42 to −55	FL 290 (8.8 km)	FL 340 (10.3 km)	1.5	7	All ice
27 Oct 03	−20 to −50	FL 240 (7.3 km)	FL 360 (11.0 km)	1.2	6	Multiphase
20 Nov 03	−44 to −49	FL 320 (9.7 km)	FL 340 (10.3 km)	0.8	7	All ice
3 Dec 03	−22 to −47	FL 230 (7.0 km)	FL 330 (10.0 km)	2.0	17	Multiphase
17 Dec 03	−15 to −17	FL 190 (5.8 km)	FL 200 (6.1 km)	0.3	2	All liquid
17 Dec 03	−38 to −41	FL 270 (8.2 km)	FL 290 (8.8 km)	0.5	3	All ice

Total missions	Maximum temperature range	Cloud-base range	Cloud-top range	Total duration (h)	Total legs	
17	−15 to −60	FL 160 to FL 320 (4.9–9.7 km)	FL 200 to FL 390 (6.0–12.0 km)	20.7	133	

* Cloud top and base temps unknown.

ceiling of the Learjet; however, occasionally a requested altitude was unavailable due to restrictions imposed by Air Traffic Control.

Table 2 lists cloud top elevations, temperatures, and duration in cloud for the 17 wave clouds investigated. The clouds have been segregated as follows.

- Five of the clouds had cloud base with temperatures equal to or colder than −40°C and did not contain any detectable supercooled liquid water (SLW). These are identified as "All ice" in Table 2.
- Eleven of the clouds contained specific regions of only SLW, mixed phase, and all ice. They had bases with $-29°C \leq T \leq -17°C$ and tops with $-60°C \leq T \leq -34°C$, except for two clouds in which the Learjet was unable to document cloud-base and cloud-top temperatures due to restrictions imposed by Federal Aviation Administration Air Traffic Control. These are identified as "Multiphase" in Table 2.
- One thin cloud had a base at −15°C and a top at −17°C and contained only small water drops. This is identified as "All liquid" in Table 2.

4. Description of wave clouds

a. Real versus simulated wave clouds

This section discusses the general similarities and differences between a wave cloud predicted using a sim-

plistic numerical model and observations of actual wave clouds. In later sections, we show in situ data that support the features described in this section. Figure 2 shows two representations of multiphase wave clouds. Figure 2a is taken from HM93 and is the result of a wave cloud model calculation using simple microphysics. Figure 2b is an illustrated representation of a wave cloud, based on observations that highlight a number of similarities and differences from the simulated cloud. In the numerically simulated cloud all of the results are predicable. Water condenses to form SLW, then freezing occurs via both homogeneous and heterogeneous nucleation processes forming a mixed-phase region followed by a glaciated cloud region. However, some aspects of these processes are less predictable and more complex in the actual wave clouds (Fig. 2b). Some of the complexity can be explained through physical arguments, while other features appear to defy explanation. Some aspects that are generally consistent within the wave cloud dataset are discussed next, followed by examples of features that are not surprising but lack consistency between clouds. Finally, some aspects of wave clouds that are currently difficult to explain are discussed.

Both Figs. 2a and 2b show that mixed-phase regions are preceded by regions with only SLW and followed by glaciated regions. As air moves upward and expands, it looses energy and cools, the saturation vapor pres-
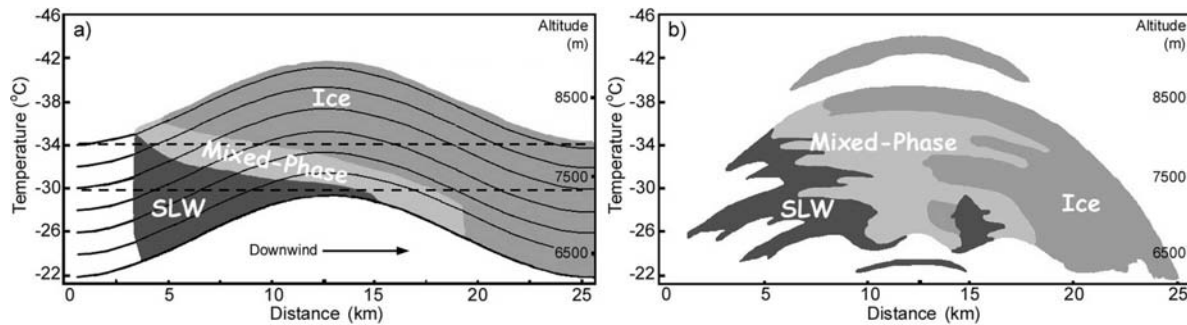
FIG. 2. (a) Numerical model of a wave cloud adapted from HM93 showing regions of supercooled liquid water, mixed phase, and ice cloud, and (b) schematic drawing showing actual variability often observed in wave clouds.

sure decreases and condensation forms supercooled water droplets. Ice phase is nucleated for some particles and SLW is converted to ice via the Bergeron–Findeisen (BF) process (Pruppacher and Klett 1997), and via accretion (riming) when conditions are suitable, leaving eventually only ice. This consistent trend in wave clouds is what motivates calling wave clouds natural laboratories and studying them as such. Some aspects of wave clouds that are generally explainable and consistent from cloud to cloud are 1) the shape of the particle size distributions (PSDs) that, in the lower cloud regions, tend to be bimodal due to the cloud physical processes of collision and coalescence and, in mixed phase, the BF process; 2) the generation of wave clouds via gravity waves, that is, atmospheric waves with a wavelength equal to wind speed divided by the Brunt–Väisälä frequency; 3) some aspects of the transition to ice signature; 4) the along-the-wind variations in the bulk properties of IWC, effective radius, radar reflectivity, SLW droplet concentration, and, in the colder clouds, ice concentration; and 5) the trend that mass contents, liquid and ice, tend to decrease with decreasing temperature. Each aspect is discussed in more detail in the following sections.

Figure 2b shows considerably more variability in the vertical direction than Fig. 2a. Most of the deep wave clouds observed in this study consisted of more than one visually identifiable cloud layer separated by clear air, or very thin cloud, above and below. One wave cloud system investigated on 3 December 2003 consisted of a stack of six distinct layers. It is expected in a moving stably stratified fluid, such as in the atmosphere where wave clouds are forming, that mixing has been inhibited in the vertical compared to the horizontal. Therefore, the multilayered structure seen in many wave clouds, while more complex than the ideal wave cloud in Fig. 2a, is not a surprise. If the vertical profile of water vapor content as well as temperature is known, then a model could predict a cloud's layered structure.

However, the structure of each wave cloud layer may be different. For example, depending on whether the air is saturated with respect to ice or not, the cloud may evaporate totally on the downward part of a wave (as depicted in Fig. 2b) or ice may remain downwind of the wave (as depicted in Fig. 2a). Additional cloud layer variability can depend on properties of the air established upwind of the clouds, on the amplitude of the wave, and other physical factors, including wind speed and turbulence intensity. Other characteristics that vary considerably from layer to layer are the magnitudes of the bulk properties of IWC, effective radius, SLW droplet concentration, ice concentration in the colder clouds, and radar reflectivity. Each of these, along with the presented data, will be discussed in more detail in section 4e.

Certain observations of the wave clouds, some of which are reflected in differences in the numerically simulated cloud (Fig. 2a) and the illustrated cloud in Fig. 2b, are more difficult to interpret. These characteristics include 1) distance from the cloud leading edge to detection of the first ice particle, 2) ice particle concentration in multiphase clouds, 3) aspects of the glaciation transition signature, and 4) aspects of the dynamical structure, namely the occurrence of shorter waves within the main wave and multiple mixed-phase regions at a given altitude. The first three items are generally related to the process of ice nucleation, which is currently an important area of research in cloud physics and one of the motivating questions for studying wave clouds as natural laboratories.

Ice crystal habits in wave clouds will also be presented and discussed. Trends are generally consistent with recent laboratory models of ice growth in the atmosphere with slight deviation.

b. Dynamical structure of wave clouds

An ideal "natural laboratory" wave cloud sits fixed in space while air flows through it: first gradually upward
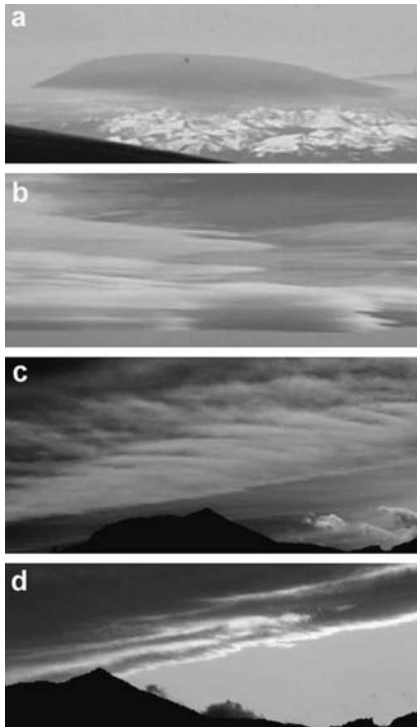
FIG. 3. Pictures of mountain-induced wave clouds that show the variability that can exist in all three spatial directions. Photographs taken from an aircraft over Utah with (a) looking most like an ideal wave cloud and (b) showing typical vertical layering. (c), (d) Photographs taken from the ground in Boulder, CO: In (c) there is wavelike structure in the direction perpendicular to the main mountain-induced wave and in (d) scattering of light from the setting sun brings out the wavelike structure near the cloud's leading edge. These waves are parallel to the main mountain-induced wave but of smaller wavelength.
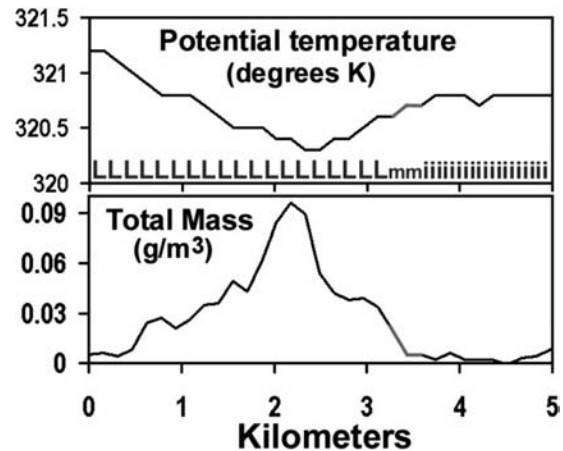

FIG. 4. Potential temperature and total condensed mass content as a function of distance downwind of the cloud leading edge for a particularly simple wave cloud. The letters L, m, and i approximately designate regions of liquid, mixed, and ice-phase cloud, respectively. The mixed-phase regions are also indicated using gray traces.

where condensation of water occurs, then gradually downward where evaporation occurs. The cloud can remain for some time in a somewhat steady-state situation. The microphysical process whereby water vapor is converted to drops and then to ice can be thought of as progressing in time for a Lagrangian parcel, but only in space from a Euclidian point of view. There is therefore an opportunity to map out the cloud with aircraft penetrations. Even the effects of the aircraft on the cloud, such as aircraft-produced ice particles (Rangno and Hobbs 1983), can be avoided by waiting for new air to flow through the cloud between penetrations.

Two main factors complicate the ideal picture described above. First, it is difficult for an aircraft to follow actual streamlines and thus measurements generally cut across streamlines and observations are not of a Lagrangian parcel. Second, wave clouds often have significantly more internal structure than expected, as depicted in Fig. 2b. Figure 3 consists of cloud photographs

with the point of showing examples of that structure. All of these clouds formed over mountains and follow the basic scenario describing wave cloud formation (i.e., Fig. 2a). One picture shows a simple wave cloud of uniform appearance while the others show the variability that often exists in the vertical and both horizontal directions.

Time series of cloud properties reveal the same variety in wave clouds, ranging from smooth and simple, as shown for example in Fig. 4, to very complex and jumbled, as shown in Fig. 5. In this paper we use the term "jumbled" to mean that regions of SLW, mixed phase, and ice do not occur in only one sequential pattern within the cloud, but instead, appear in multiple regions when viewed from the perspective of a constant-altitude aircraft cloud penetration. For a level penetration through an ideal wave cloud the potential temperature should gradually decrease and then increase again while the condensed mass content would increase and then decrease gradually. This picture is close to what is seen in Fig. 4. In contrast, Fig. 5 reveals a much more complex structure. There are two long waves of about 15-km length. The first long wave has an additional oscillation superimposed with a wavelength of about 1.2 km. The second large wave, which is primarily glaciated, also has large variations but with less regularity. The wind speed divided by the Brunt–Väisälä frequency, calculated from a nearby sounding, gives the characteristic wavelength of a gravity wave, which yields a wavelength of about 15 km in clear air. This explains the long waves. However the 1.2-km wavelength oscillation seen in the first 15 km, and the
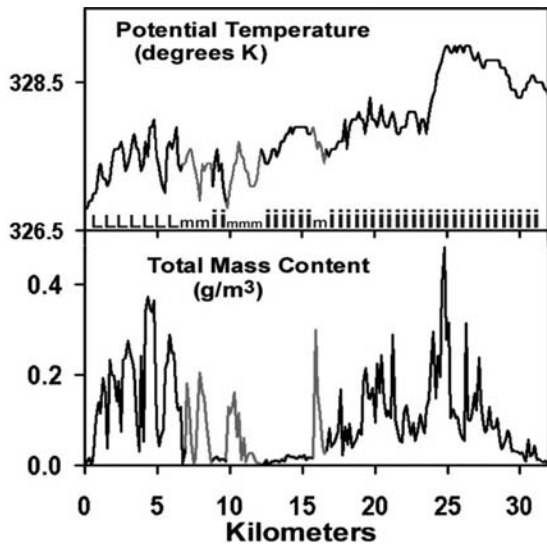
FIG. 5. As in Fig. 4 except for a particularly complex wave cloud.

more random variability seen in the last 15 km, of Fig. 5 are more difficult to interpret. It is possible that vertical velocity and relative humidity measurements would shed light on this issue. However, it is more likely that, if those measurements had reliably been made, they would be consistent with the wave structure inferred from the IWC and potential temperature without yielding insight as to the cause of that structure. We present these data on the complex dynamical structure of wave clouds because it is important with regard to other microphysical interpretations of the clouds. We do not, however, attempt to explain the cause of the complex structure.

The example shown in Fig. 4, where the wave is smooth, and the example in the first 15 km of Fig. 5, where the wavelength is equal to that of a gravity wave with shorter waves superimposed, are atypical of most of the cases in our dataset. Instead, most of the waves in the dataset are neither smooth nor periodic but are rather more like the second 15 km of Fig. 5. The amount of structure varies from cloud to cloud. Additional examples of time series are shown later in section 4c. Clouds that have single SLW and mixed-phase regions, that is nonjumbled clouds as defined above, are most suitable for studies of "wave clouds as a natural laboratory." In section 5, the onset of riming is studied using four such clouds.

c. Spatial trends in two dimensions

This section presents and discusses spatial trends in the horizontal (x, along the wind direction) and vertical (z) directions of a wave cloud with single regions of

SLW and mixed phased (i.e., not jumbled). Figure 6 shows an x–z cross section of the microphysical characteristics of a multiphase wave cloud with single regions of SLW and mixed phase investigated on 20 October 2001. This was a relatively deep wave cloud; thin regions of clear, or nearly clear air, existed in between what appeared to be three distinct cloud layers. The cross section is a combination of actual measurements made at the levels indicated and generalizations based on this and the other multiphase clouds. There was one, but only one, repeat penetration at the same location and altitude in this cloud. The two penetrations were about 45 minutes apart in time and at −36°C. The location of the cloud itself had not changed significantly. Also the overall microphysical characteristics were the same for both penetrations. Individual features were not identifiable from one penetration to the other, as expected, given the time delay. A vertical profile showing examples of CPI images, maximum particle size, particle concentration, and IWC, at about longitude 104.7° in Fig. 6, is shown in Fig. 7. IWC was measured by the Nevzorov TWC probe and also inferred using particle data from the FSSP, CPI, and 2D-C probes using the method of Baker and Lawson (2006). The figure shows that there is reasonable agreement of IWC measured using the two techniques. However, this is not always the case throughout our dataset. Sometimes the agreement in IWC is very poor, as might be expected since the Baker and Lawson (2006) analysis was based on the Mitchell et al. (1990) dataset that was collected at the surface in the Sierra Nevada, and is not necessarily representative of all crystal types. Both IWC measurement techniques are subject to large undetermined uncertainties. A rigorous comparison of IWC measurements is not the focus of this paper; rather, it is the location of the relative maximum that is significant.

Figure 8 shows time series of microphysical measurements from nine selected Learjet penetrations of multiphase wave clouds. The examples have been selected to show the variability in the measurements, as well as to show trends. Figures 5–7 reveal some of these trends, most of which are common to all the multiphase clouds. Several of these cloud features are expected based on physical arguments:

1) SLW exists only at temperatures warmer than about −37°C, which is close to the homogeneous freezing temperature of pure water;
2) a transition occurs along the wind direction from SLW to mixed phase and then to glaciated cloud, as discussed in section 4a;
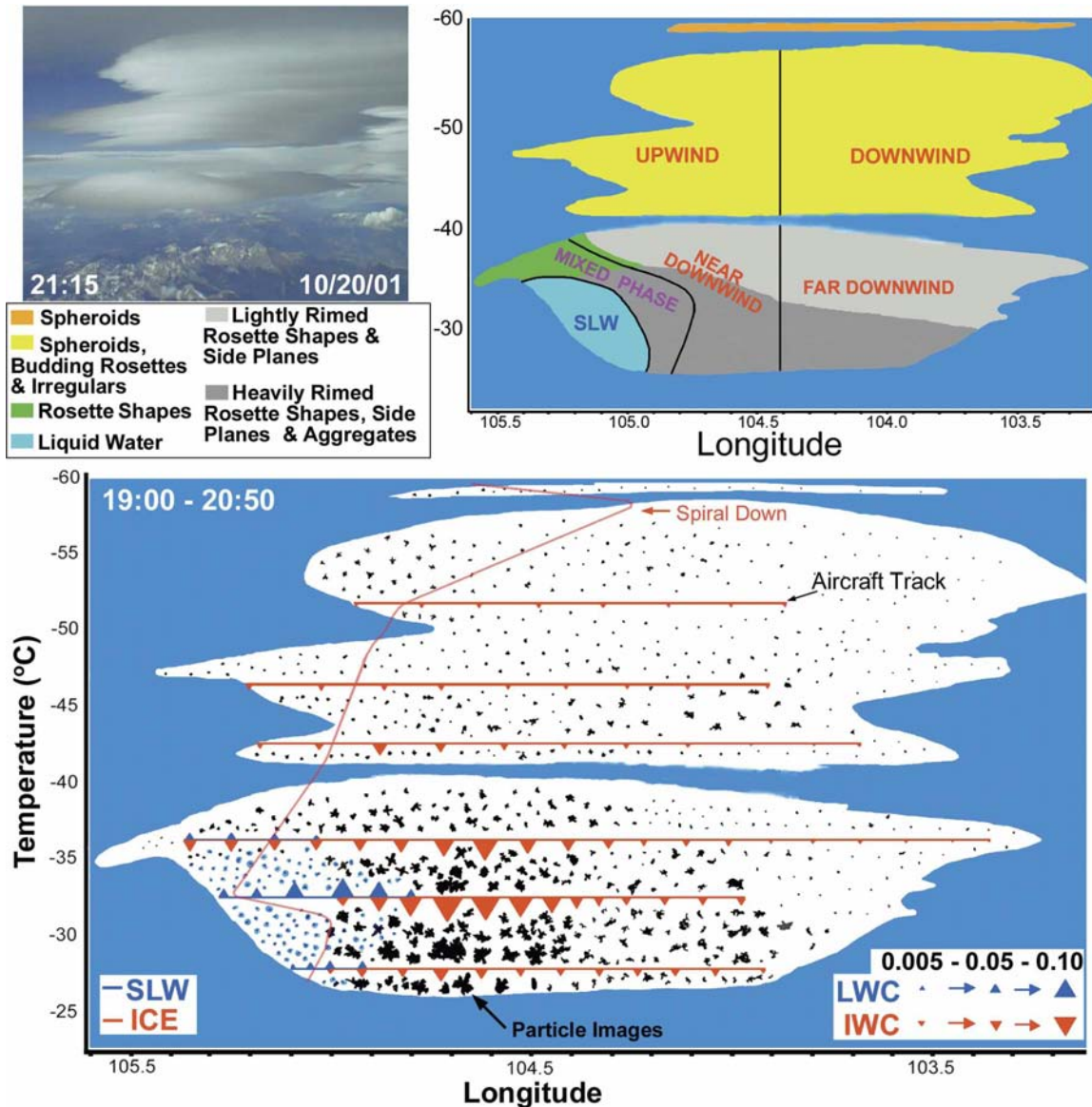3) a SLW content maximum in the wind direction is

FIG. 6. Cross section showing (top left) a photograph of the wave cloud system taken 25 min after the wave cloud was investigated by the SPEC Learjet on 20 Oct 2001, (bottom) a schematic representation of microphysical properties (see legend at bottom of panel), and (top right) generalized regions also showing the locations of typical particle types in this and other multiphase wave clouds (see legend at left of panel).

near the transition to mixed phase because this location is generally within the updraft region just before LWC decreases due to conversion to ice;

4) mass content increases with increasing temperature because warmer air has greater moisture capacity, and upward transport is too limited to transport significant mass to colder temperatures, such as can occur in cumulus clouds.

5) the largest particles are found low in the cloud due to higher mass contents at that location, and precipitating particles low in the cloud have experienced a

longer time for growth by vapor diffusion, riming, and ice aggregation;

6) aggregation lower in the clouds can explain the observation that particle concentration maximums are found higher in the clouds than the IWC maximums;

7) along the wind direction downwind of the SLW-only region, ice particles become increasingly more rimed and covered with side plane as SLW is converted to ice in the mixed-phase cloud. This process often occurs to the extent that the original underlying crystal type is unrecognizable. Farther down-
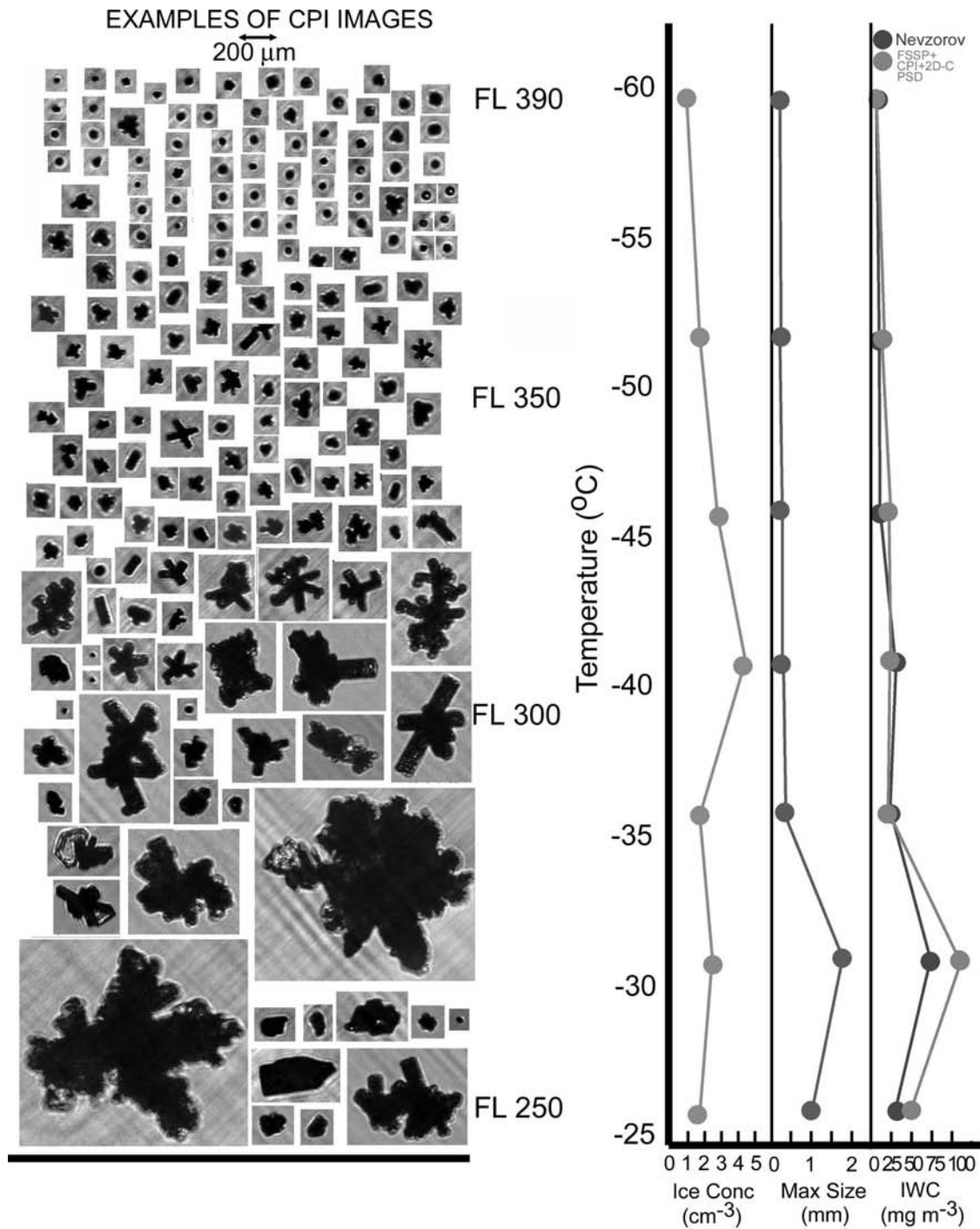
FIG. 7. Vertical profile showing examples of CPI images and microphysical data in a wave cloud just downwind of the mixed-phase region (at about longitude 104.7° in Fig. 6). The values of ice particle concentration (Ice Conc), maximum particle size (Max Size), and ice water content (IWC) are 10-s (1.5 km) averaged values.

wind, beyond the mixed-phase regions, rounded irregular shapes that often have narrow ice bridges connecting larger features are observed, similar to ice particles observed in sublimating regions by Korolev and Isaac (2004).

Figure 6 also depicts the generalized regions: SLW, mixed phase, near downwind, far downwind, upwind, and downwind. PSDs, habit class percentages, and bulk microphysical properties will all be shown averaged over these generalized regions. The SLW and mixed-
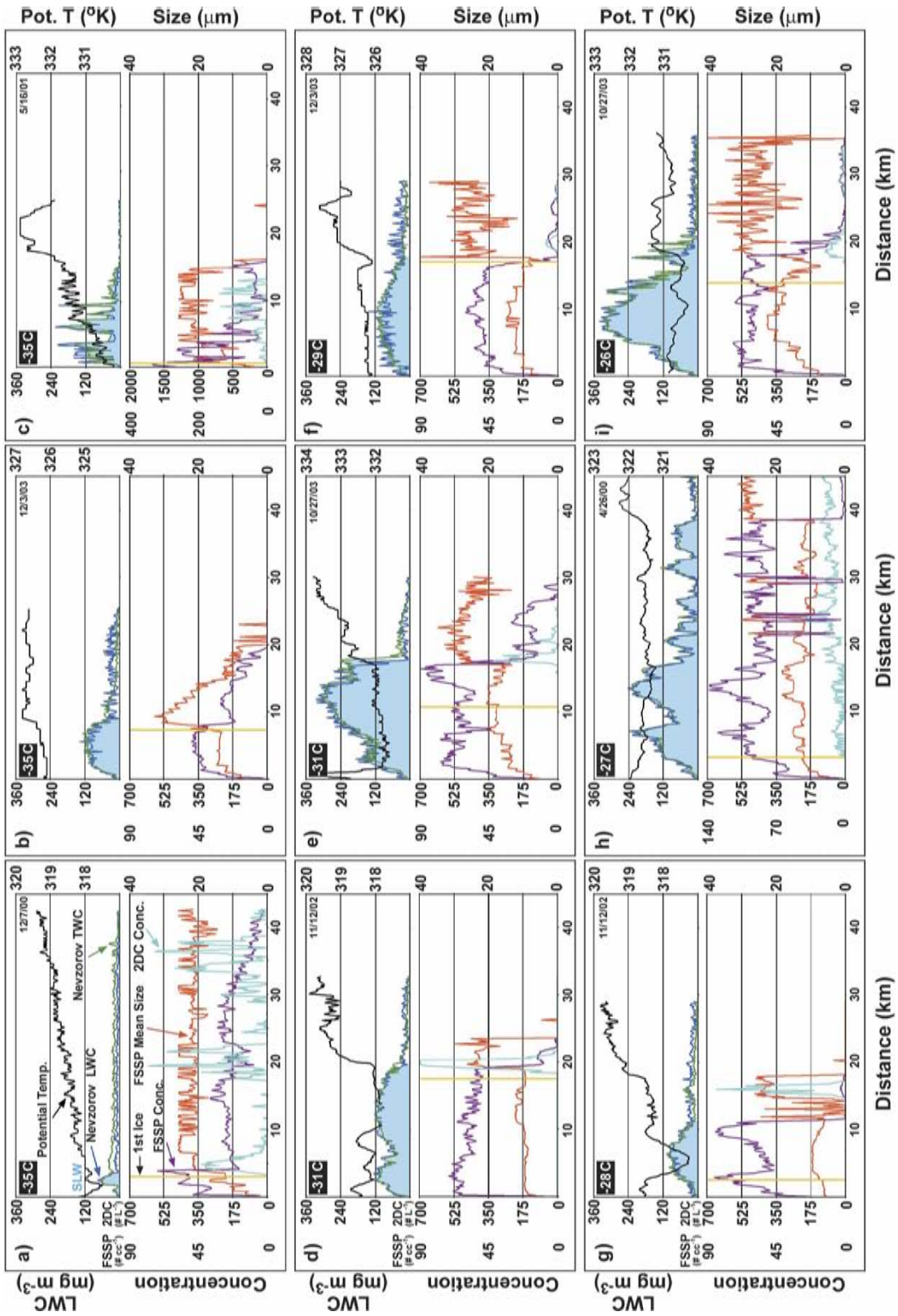
FIG. 8. Plots of microphysical parameters *vs* distance from leading edge of multiphase regions of wave clouds. Key in (a) applies to all panels. SLW region defined by a Rosemount icing probe is shown as light blue fill. First observed ice particle is marked by a vertical yellow line.

phase regions are easily distinguished based on the phase(s) of water present. The distinction between near versus far downwind, and the distinction between upwind versus downwind, are less exact. Because of the lack of vertical velocity and relative humidity measurements, particle sizes were used to find the boundary between these regions. The intention was to set the boundaries where the particle sizes were maximum so that it roughly represents where sublimation became significant.

d. Ice nucleation

The vertical yellow line in Fig. 8 shows the location where the first ice particle was detected, based on careful visual analysis of 2D-C and CPI images. The same glaciation transition signature, as observed by both HM93 and F01 and described above in section 2, is very common in the Learjet dataset and a number of examples are shown in Figs. 8a, 8d, 8e, 8f, 8g, and 8i. At the point where the Rosemount icing detector (light blue shading under the darker blue Nevzorov LWC trace) indicates the cessation of detectable SLW, there is simultaneously a decrease in FSSP concentration (violet trace) and an increase in both 2D-C concentration (light blue trace) and FSSP mean size (red trace). The reduction in FSSP concentration and increase in FSSP mean size is explicable since the smallest particles, liquid drops, have just evaporated, leaving the fewer but larger ice particles that were growing at the expense of the liquid. At the airspeed of the Learjet in these wave clouds (average of ≈ 160 m s^{-1}), the 2D-C, measures ice particles greater than approximately 150 μm (Lawson et al. 2006a). The 2D-C images have been examined to eliminate "streakers" caused by streaming water. The observed trend for 2D-C concentration to increase rapidly at the glaciation transition has not been explained as either a physical process or a spurious instrument effect. It suggests that ice nucleation is greatly enhanced just as the droplets evaporate. This allows for hypotheses based on a number of physical effects, which will be discussed in subsequent paragraphs.

Another observation that suggests a possible lack of full understanding of the ice nucleation process is the poor correlation between temperature and ice concentration. The lack of correlation is shown in Fig. 9, where the average ice concentration is computed for 23 Learjet penetrations in multiphase clouds in the regions just downwind of where the SLW ends abruptly. The data are averaged over the first significant peak or the first few peaks in ice concentration. Similar, and also shown in Fig. 9, is the lack of correlation between temperature and the distance from the cloud leading edge to the location of the first detected ice. While we have sug-
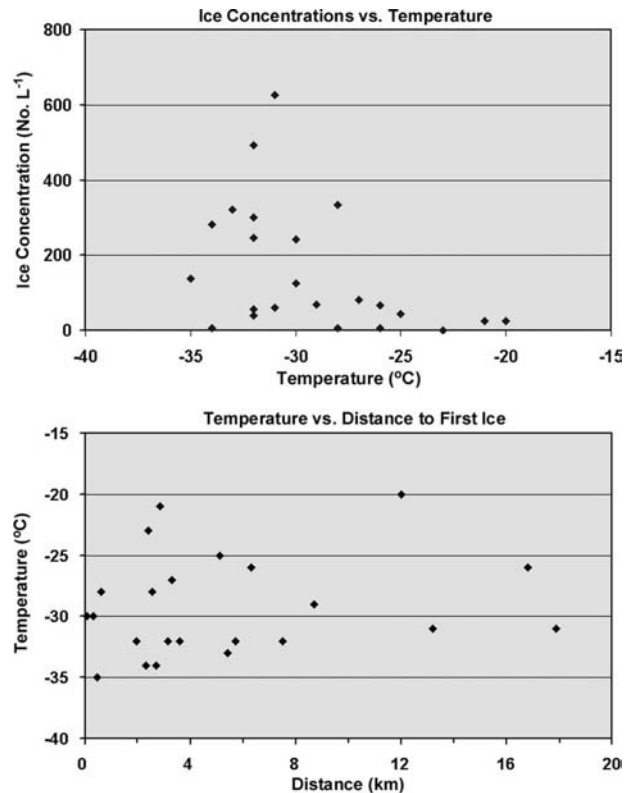

FIG. 9. Scatterplots of (top) 2D-C ice particle concentration vs ambient temperature and (bottom) ambient temperature vs distance from cloud leading edge to location of first ice.

gested that the poor correlations result from a lack of understanding of the nucleation process, there are other possible explanations. The variability in the measurements leading to the poor correlations seen in Fig. 9 could be due to unknown, but physically explainable, characteristics of the cloud condensation and ice nucleation aerosol entering the clouds, and/or vertical velocity characteristics that were not measured.

The glaciation transition signature was very common in the Learjet dataset. There are some understandable exceptions and these are shown in Figs. 8b, 8c, and 8h. In Fig. 8b the 2D-C ice concentration is very low throughout and yet the typical signature of decreasing FSSP concentration and increasing mean size is still observed at the point where the SLW ceases. This can be explained by the fact that particles must be at least 150 μm in size before the 2D-C can detect them at jet aircraft speeds (Lawson et al. 2006a). The vertical motions were likely too weak to grow such large particles in this cloud. In Fig. 8c the 2D-C ice concentration increases significantly about 1 km from the leading edge (note 2D-C concentration scale change in this panel only), FSSP concentration decreases and mean size increases as expected, but the SLW continues

downwind for about 10 km. Figure 8h shows an example of a penetration at $-27°C$ where ice, in high concentration, is observed starting about 3 km from the leading edge, continuing throughout the SLW region for about 40 km, until the typical FSSP transition signature is observed, coincident with cessation of SLW. These exceptions can be understood as both of these clouds are examples of jumbled wave clouds with shorter than expected waves within the main wave cloud, similar to the exceptional case shown in Fig. 5. Presumably the transition, or rather evaporation, occurred more than once (for a Lagrangian parcel) in these clouds and we observed different parts of the signature at different locations.

It is worth pointing out that five examples in Figs. 8d, 8e, 8f, 8g, and 8i are at temperatures too warm, $-26°$ to $-31°C$, for homogeneous nucleation. In addition, for these five cases the possibility was examined that homogeneous nucleation occurred aloft at temperatures $<-37°C$, and the ice that was formed followed streamlines down to the observation level. This was considered by examining the coldest ambient temperature with the same potential temperature as the observation level. The coldest ambient temperatures were at most $2°C$ colder than the temperatures at which the ice was observed. This argues against homogeneous freezing aloft for these five cases. SLW drops may have also experienced cooling from evaporation. Our cryogenic hygrometer measurements show a rapid decrease in relative humidity where the SLW ends and ice forms but, unfortunately, the absolute value of the measurements are not sufficiently reliable. However, HM93 and F01 have shown that the relative humidity will reduce from water to ice saturation in the region with rapid ice production, and the difference in the wet-bulb and frost-bulb temperatures is only about $0.5°C$ (Cooper 1995). Thus, neither homogeneous freezing via evaporation to the classic frost-point temperature and/or ice descending from colder regions aloft are likely explanations.

Cooper (1995) considered possible physical mechanisms that could explain the rapid ice formation when supercooled drops evaporate. One explanation is based on the hypothesis of Beard (1992), that the residues left by evaporating droplets may act as "evaporation ice nuclei" and produce high concentrations of ice. Cooper points out that, if this mechanism were operating unless the activation mechanism is very short lived, repeated cycling through evaporating and SLW regions of cloud (e.g., Fig. 5) should result in high ice concentrations in the leading edge of downwind SLW regions, and this has not been observed. A new hypothesis put forth by Cooper is based on a possible kinetic effect. Although

speculative, Cooper shows that, if the thermal accommodation coefficient is small enough (i.e., $<\sim0.01$) and the condensation coefficient equals 1, droplets could cool to the homogeneous freezing temperature. Shaw and Lamb (1999), however, measured the thermal accommodation coefficient of supercooled water to be very close to 1.

Young (1973) showed that a particle on the surface of a supercooled drop is a better ice nucleus than the same particle immersed in a supercooled drop. The phenomenon is called contact nucleation. Shaw et al. (2005) showed that contact nucleation appears to work from the inside as well. That is, when a particle is immersed but very near or touching the surface of a supercooled droplet, it is a better ice nucleus than when it is far from the surface. The difference in the two modes of nucleation was found to be between $4°$ and $5°C$ for all of the materials tested. This poses an interesting hypothesis on the cause of the observations that ice nucleation is greatly enhanced just as the wave cloud droplets evaporate (Durant and Shaw 2005). When a particle is first condensed upon at the leading edge of a wave cloud, the solute effect will inhibit ice nucleation if there is a soluble part. As the droplet grows larger, the addition of mass at the surface will make it very unlikely for any insoluble part to be near the surface even while Brownian motion moves the particle away from the center. As the droplets approach small sizes during evaporation, the probability of a particle being near the surface increases greatly before the size is so small that solute effects become inhibitive to nucleation. At this point the increased ice nucleating ability may be high enough to explain the observations of enhanced ice nucleation as the droplets just evaporate. Figure 8h shows an exception to the general observation reported by F01, which is that significant ice is not observed until after the cloud droplets have reached their maximum size. Figure 8h is an exception to the findings reported by F01 and is also an exception to the general findings from the Learjet dataset.

Another hypothesis (J. Hallett 2006, personal communication) for why droplets may nucleate ice upon evaporation is based on the properties of eutectics. Hallett (1968) shows that, when a eutectic that is doubly unstable is nucleated for one of the phases, it can initiate nucleation of the other phase. The concept for clouds is that, as a supercooled solution droplet that is also supersaturated with respect to the salt is evaporating, the point of homogeneous nucleation of the salt will be reached, thus initiating rapid precipitation of the salt and initiate freezing of the liquid in a local region of the droplet where the solute effect is suddenly drasti-
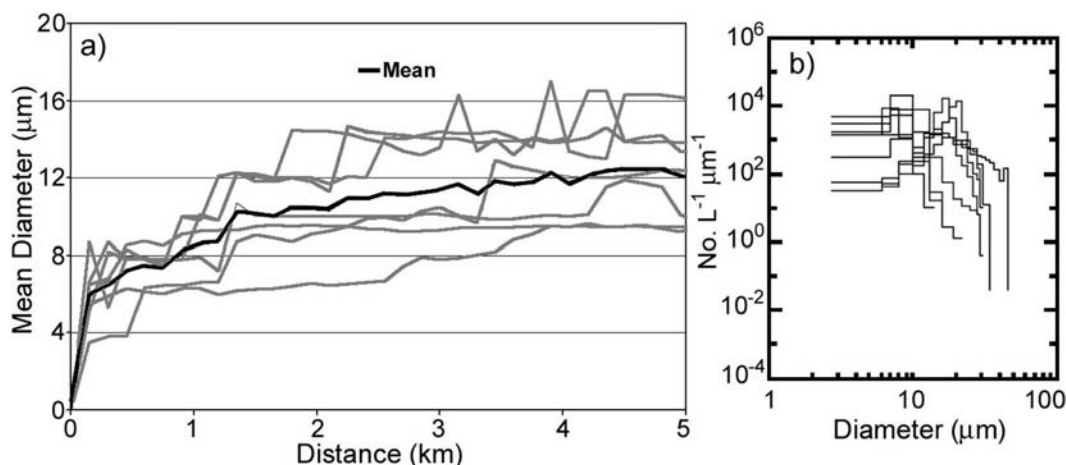
FIG. 10. Plots showing (a) FSSP mean droplet diameter vs distance from the cloud leading edge, with the average of the seven curves shown as a thick black line, and (b) FSSP drop size distributions averaged from 4 to 5 km of each time series shown in (a).

cally reduced. Laboratory modeling of this process is under way at the Desert Research Institute, but to evaluate its effectiveness in natural clouds, accurate observations of the composition of the aerosol on which ice has nucleated in evaporating regions of natural clouds is also necessary.

The data shown in Fig. 8 demonstrate both the variability and consistency in microphysical properties of wave clouds. There is considerable consistency in the "glaciation transition signature" pattern; that is, a significant increase in 2D-C ice concentration is usually coincident with the location where the SLW ends, FSSP mean size increases, and FSSP concentration decreases. While the decrease in FSSP concentration and increase in mean size at the glaciation transition is understandable, the rapid increase in 2D-C concentration is a topic for speculation. There is also consistency in that the first ice is generally not observed prior to the location in the SLW region where the FSSP drop size reaches its maximum value. However, as detailed above, in this large dataset there are exceptions to each of these general trends.

e. Bulk microphysical properties

Figure 10a shows the growth of cloud drops starting from the leading edges and progressing downwind in the SLW regions of seven wave cloud penetrations that had SLW with minimal or no ice for at least the first 5 km of the penetration. The FSSP mean diameter is plotted as a function of distance from the leading edge to 5 km downwind. The drops grow rapidly to a diameter of about 6–8 μm within the first few hundred of meters from the leading edge and increase to a final diameter of about 9–16 μm. In a few cases, mean drop diameters

reached or exceeded 20 μm farther downwind than 5 km (e.g., Figs. 8e and 8i). Figure 10b shows seven FSSP drop size distributions, the average between 4 and 5 km of each time series shown in Fig. 10a. As expected, the initial growth of the cloud droplets is monotonic and droplet size distributions are narrow. There is some variability between clouds, presumably due to vertical velocity differences and perhaps CCN differences. It is noteworthy that seven penetrations exist with so little ice observed in the first 5 km or more, and that most penetrations have significant regions with SLW and no observations of ice. This suggests that deposition ice nuclei were rare and of little significance.

Table 3 shows the mean, standard deviation, and extreme values of optical extinction (β_{ext}), particle concentration, LWC, IWC, radar reflectivity, and two values of effective particle radius (R_{eff_a}) and (R_{eff_b}) for each of the generalized regions of wave cloud defined in Fig. 6. Here β_{ext} is calculated as twice the area of each particle's two-dimensional projected image, summed over all of the particles in a sampled volume, divided by the sampled volume. Radius R_{eff_a} is calculated as the third moment of the size distribution divided by the second moment of the size distribution; R_{eff_b} is calculated as IWC, using the method of Baker and Lawson (2006), divided by extinction with the appropriate multiplicative factor such that $R_{eff\_b} = R_{eff\_a}$ for solid spherical ice particles. For nonspherical particles the two values can be quite different due to the CPI and 2D-C contributions, which do not involve spherical assumptions for estimating mass or area. The number of aircraft passes in each region is also given. The data from the all-ice clouds are combined with the data from the colder than −37°C regions of the mul-

TABLE 3. Statistics computed for leg-averaged values of parameters shown within regions identified in Fig. 6.

SLW, $N = 33$	Mean	Std dev	Max	Min	Far downwind ($T \geq -37°C$), $N = 23$	Mean	Std dev	Max	Min
β_{ext} (km^{-1})	3.88	3.77	17.1	0.38	β_{ext} (km^{-1})	4.78	3.87	17.53	0.30
R_{eff_a} (μm)	4.1	1.8	7.9	2.1	R_{eff_a} (μm)	65.2	60.5	230	12.0
R_{eff_b} (μm)	4.1	1.8	7.9	2.1	R_{eff_b} (μm)	33.0	14.9	61.8	11.9
Reflectivity (dBZ)	−41.3	−37.5	−68.4	−30.4	Reflectivity (dBZ)	−7.3	−4.2	−0.5	−28.9
Concentration (cm^{-3})	73.3	59.2	244	14.2	Concentration (cm^{-3})	5.1	7.2	28.5	0.6
LWC (g m^{-3})	0.025	0.025	0.117	0.003	IWC (g m^{-3})	0.092	0.077	0.327	0.006

Mixed phase, $N = 30$	Mean	Std dev	Max	Min	Upwind ($T \leq -37°C$), $N = 25$	Mean	Std dev	Max	Min
β_{ext} (km^{-1})	12.05	13.01	68.61	0.76	β_{ext} (km^{-1})	2.26	1.96	6.61	0.23
R_{eff_a} (μm)	30.7	31.2	148	4.3	R_{eff_a} (μm)	14.8	7.5	40.1	7.8
R_{eff_b} (μm)	18.3	9.9	42.7	4.0	R_{eff_b} (μm)	13.6	5.0	26.7	7.8
Reflectivity (dBZ)	−7.5	−4.5	1.6	−41.0	Reflectivity (dBZ)	−27.1	−23.7	−17.3	−44.3
Concentration (cm^{-3})	45.7	32.1	114	4.6	Concentration (cm^{-3})	6.1	6.9	29.3	0.5
IWC (g m^{-3})	0.115	0.102	0.315	0.006	IWC (g m^{-3})	0.017	0.015	0.056	0.002

Near downwind ($T \geq -37°C$), $N = 35$	Mean	Std dev	Max	Min	Downwind ($T \leq -37°C$), $N = 19$	Mean	Std dev	Max	Min
β_{ext} (km^{-1})	8.03	6.59	31.40	0.72	β_{ext} (km^{-1})	3.15	3.86	16.62	0.14
R_{eff_a} (μm)	61.2	65.9	248	12.2	R_{eff_a} (μm)	12.8	3.9	21.6	6.4
R_{eff_b} (μm)	29.4	15.0	64.4	12.1	R_{eff_b} (μm)	12.5	3.7	22.5	6.4
Reflectivity (dBZ)	−4.8	−1.5	4.7	−26.8	Reflectivity (dBZ)	−29.5	−28.3	−22.9	−46.4
Concentration (cm^{-3})	9.7	10.0	41.2	1.0	Concentration (cm^{-3})	8.4	9.2	27.1	0.4
IWC (g m^{-3})	0.129	0.098	0.367	0.006	IWC (g m^{-3})	0.022	0.029	0.126	0.001

tiphase clouds. The average ice particle concentrations in the lower, warmer than −37°C, regions, are of the same order of magnitude as those reported by F01, using measurements from a small ice detector (SID) and counterflow virtual impactor (CVI), but much higher than those reported by HM93 and HM95 using 2D-C instrumentation.

The bulk properties are computed from a composite FSSP, CPI, and 2D-C PSDs (Lawson et al. 2001). Extinction is based on the projected area of CPI and 2D-C images plus a spherical assumption for FSSP particles. IWC is computed using a new algorithm based on particle length, width, area, and perimeter of CPI images and the area of 2D-C images (Baker and Lawson 2006).[2] Radar reflectivity is computed using particle length and the technique described by Matrosov (1993, 1997).

Understandable trends are seen in the average microphysical properties of the multiphase wave clouds. In cloud regions warmer than the −37°C isotherm, the decrease in total particle concentration from region to region reflects the conversion of water drops to ice and

aggregation processes. Extinction increases with mass for a given number of particles and, for a given mass, decreases with increasing particle sizes. Therefore, extinction logically peaks where the mass peaks, or upwind of that point if significant conversion from smaller to larger particles has occurred via the BF, riming, and aggregation processes. As seen in Fig. 8, for some clouds the mass peaks in the SLW-only region and for other clouds it peaks in the mixed-phase region. On average, extinction is higher in the mixed-phase region for this dataset, as can be seen in Table 3. This indicates that particles are often still growing and mass is still increasing in the mixed-phase region, which results in peaking of average values of other parameters that also reflect particle size in this region (i.e., R_{eff_a}, R_{eff_b}, and reflectivity).

Particle concentrations and bulk properties can vary considerably in the upper cloud regions, similarly to how they can vary in lower regions (Figs. 5 and 8). However, the average particle concentrations and bulk properties do not vary as much from the upwind to downwind regions in the upper wave cloud regions (colder than −37°C) as they do in the lower cloud regions. We attribute this to an absence of SLW, and thus particle growth via the BF process, and minimal aggregation due to small particle sizes. Values of IWC, extinction, and particle sizes are considerably smaller

---

[2] Except where otherwise noted, length in this paper refers to the longest chord of the 2D projected image and width refers to the longest chord perpendicular to the length-defining chord.

than in the warmer cloud regions. This is because the total condensable water content decreases with temperature, as expected from the Clausius–Claperon equation. The above description applies to both the all-ice clouds (Table 2) and the all-ice regions (colder than $-37°C$) of the multiphase clouds. The particle characteristics in both all-ice regions were found to be similar and were therefore combined in the calculations for Table 3. The observations are consistent with and similar to HM95's observations of cold clouds. However, the current study does not have instrumentation capable of measuring particles with diameters $<3 \mu m$ needed to infer the occurrence of homogeneous freezing (HM95). The same trend of higher mass contents with warmer temperatures, mentioned above, can also be seen in Fig. 8. Since the maximum mass content also depends on the amplitude of the wave, the trend is not monotonically related to temperature.

It is noteworthy that, while the upwind to downwind trends and temperature trends discussed above for bulk microphysical properties are understandable via basic cloud physics and are in part reflected in the averaged properties, the large standard deviations reported in Table 3 indicate the considerable variability in bulk properties from one wave cloud to another due to naturally varying environmental conditions.

f. Particle size distributions

Figure 11 shows PSDs averaged over the same regions of multiphase wave clouds as the bulk properties shown in Table 3. The region-averaged PSD for each of the N legs is shown as well as the average of those N PSDs. The warmer regions have larger particles, as also shown in Table 3. The largest particles are often the result of riming and aggregation, which is much more prevalent in the warmer cloud regions.

Figure 11 shows that the average PSDs are bimodal in all three (mixed phase, glaciated near downwind, and glaciated far downwind) regions of wave clouds warmer than $-37°C$ that contain ice. The bimodality is most noticeable in the plots of mass versus particle size. This is understandable in the mixed-phase region. The small mode is composed of SLW droplets and the large mode is the result of ice that has grown larger via the BF and riming processes. Aggregation also contributes to the large ice mode in some clouds. The continuation of the small mode downwind into the glaciated regions of wave clouds, after the cessation of SLW, indicates that a significant number of the droplets have frozen. Apparently the majority of the drops freeze near the end of the mixed-phase region, explaining why they have not rapidly grown to larger sizes in the water-saturated environment and suggesting, as discussed above, that

ice nucleation is enhanced just before the droplets evaporate. This is consistent with the rapid rise in 2D-C ice concentration that is often observed near the end of the mixed-phase region (Fig. 8).

The result shown in Fig. 11 that single-mode PSDs with smaller particles are generally found at temperatures $<-37°C$ is understandable because cloud drops are not present (the BF process is nonexistent) and aggregation is reduced for the smaller sizes. However, a single PSD, observed at $-41°C$, does not follow the trend described above. The PSD stands out in Fig. 11 because it is bimodal, much like the majority of warmer cloud PSDs. Perhaps the aerosols on this unusual day were of such a nature as to allow solution drops to form and remain liquid at that temperature (HM95). This may conceivably facilitate some of the same processes operating in the warmer cloud regions to produce a bimodal PSD at $-41°C$. Alternatively, the updraft may have been stronger on this day, advecting characteristically warmer cloud air to colder temperatures.

g. Ice crystal habits

The adage that no two snowflakes are exactly the same may be applied to all natural ice crystals. However, the task of describing the ice crystals in wave clouds requires that we coarsely group them into categories. Averages and standard deviations of the percentages of the different categories are shown in Fig. 12. The averages are taken over all wave clouds and the regions are the same as defined in Fig. 6 and are also used in Fig. 11 and Table 3. Only particles larger than $50 \mu m$ in length are included because the difficulty in automatic classification increases with decreasing size. From the average particle size distributions (Fig. 11), we can estimate the percentages of crystals, extinction, and mass that are contained in the crystals smaller than $50 \mu m$. For the mixed-phase region particle size distributions, those percentages are 99.9%, 86.2%, and 54.3%, respectively. For the near-downwind region the percentages are less due to the disappearance of the small liquid drops. The values are 99.4%, 70.2%, and 41.7%, respectively. For the far-downwind region the percentages are further reduced to 99.1%, 54.3%, and 25.1%, respectively, due to evaporation and aggregation. For the upwind side of the upper cold region the percentages are 99.8%, 94.5%, and 84.0%, respectively. For the downwind side of the upper cold region the percentages are 99.9%, 97.8%, and 93.8%, respectively. Figure 13 shows a breakdown of the habit percentages as a function of size for all mixed-phase regions combined. In this case all crystals were included.

The categories that we chose were motivated by 1) traditional crystal habit categories as in Magono and
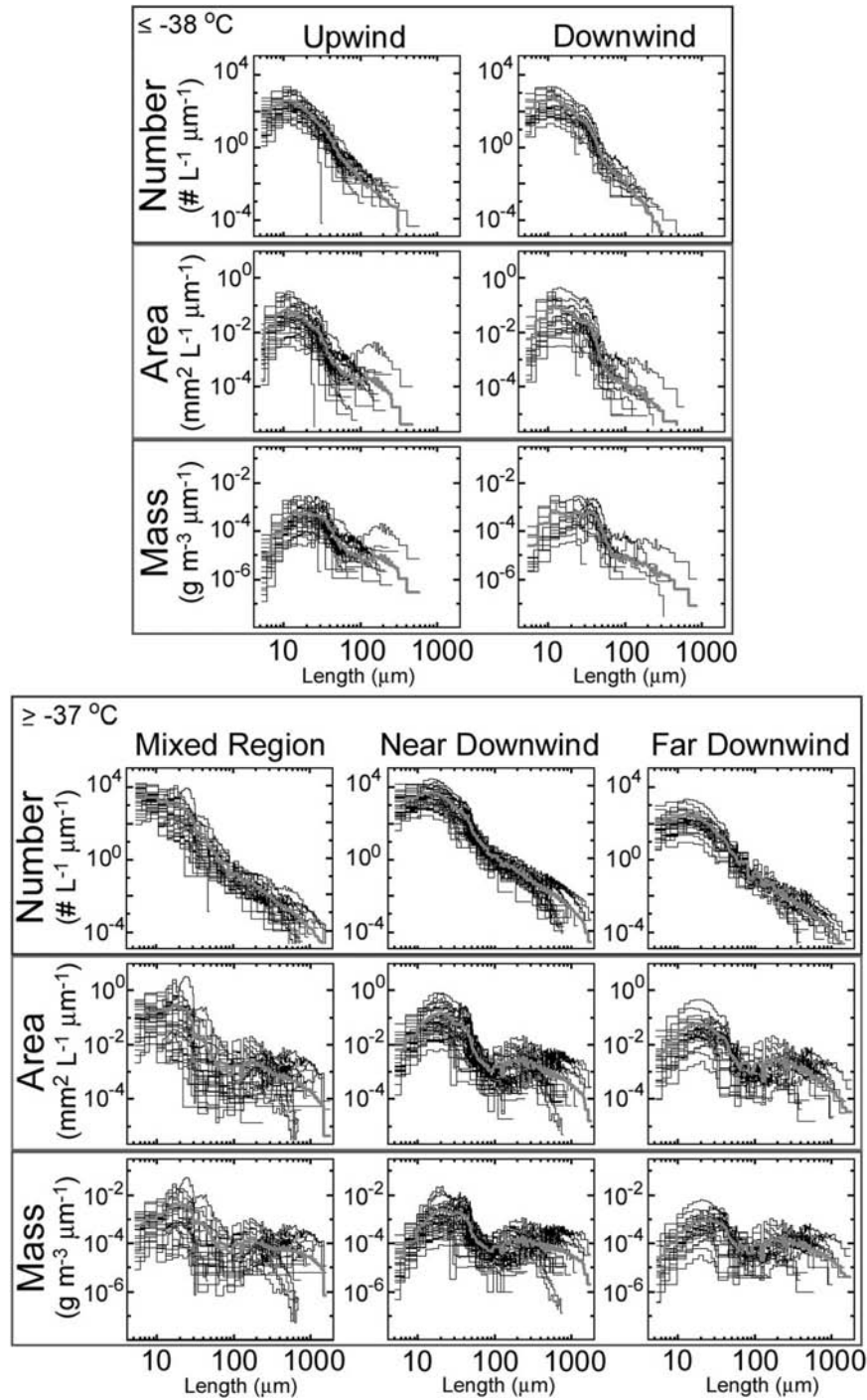
FIG. 11. Wave cloud particle size distribution weighted by number, area, and mass for two regions $\leq -38°C$ and three regions $\geq -37°C$. Wave cloud regions are labeled as depicted in Fig. 6. Each PSD shown in black is a leg average and the thicker gray line is the mean of all of the legs.

Lee (1966), 2) crystal types found in wave clouds and their general characteristics, and 3) the possibilities currently available for automatic classification of CPI images. For example, columns are a traditional habit classification but automatic classification is easier when single bullets and other crystals with high aspect ratios are grouped together with columns. So these shapes have all been grouped together and, for the sake of
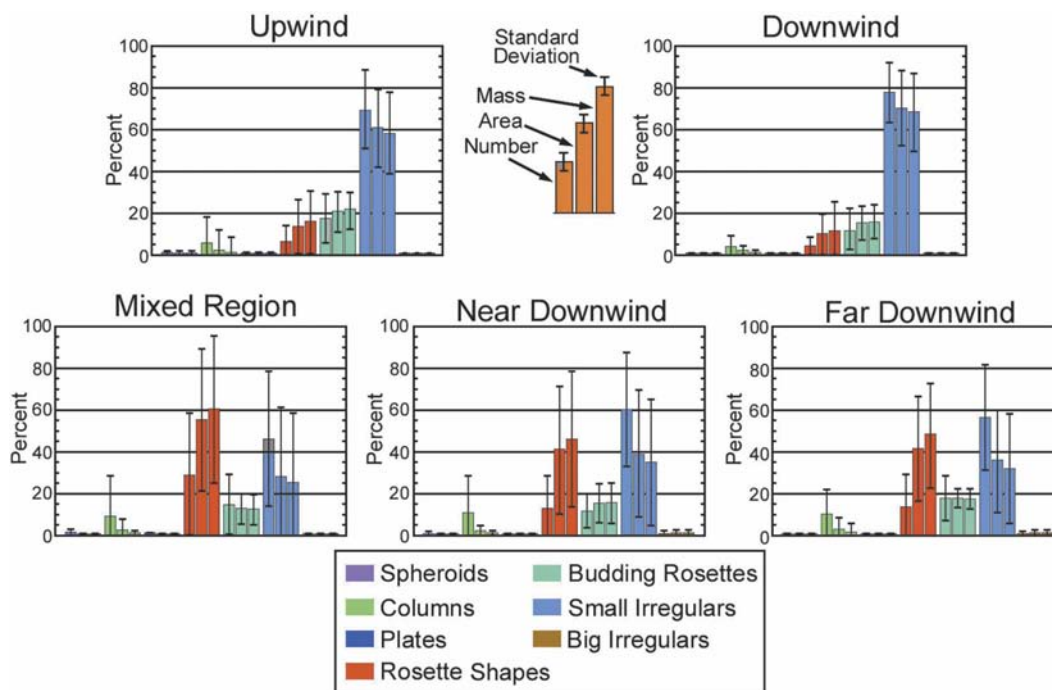
FIG. 12. Bar graphs showing mean and standard deviation of the percentage, weighted by number, area, and mass, of the different particle types discussed in the text. The regions are the same as defined in Fig. 6 and used also for Table 3 and Fig. 11. Only particles >50 μm in length have been classified.

simplicity, are referred to as columns. They are found only as minority constituents in wave clouds.

The dominant crystal type by mass in most wave clouds is the rosette shape,[3] which includes pristine bullet rosettes, mixed-habit rosettes, rosettes with side-plane, and platelike polycrystals. Bailey and Hallett (2004a) found that, in the laboratory, pristine bullet rosettes form *only* at temperatures below $-40°$C. To simulate crystal growth during fall or precipitation, Bailey and Hallett (2004b) grew bullet rosettes at $-40°$C and then observed their continued growth at warmer temperatures. Their observations showed that the pristine bullet rosette crystals continued to grow in shapes that are similar but more complex, containing side-plane and irregularly shaped appendages. Also, the component bullets experienced decreasing aspect ratios, becoming partially hollow if "fall" occurred near water saturation.

Our observations generally support the Bailey and Hallett (2004a,b) laboratory findings. The vast majority of pristine bullet rosettes are found at temperatures

below $-40°$C, while at warmer temperatures $>95\%$ of rosette-shaped crystals are not pristine, but instead contain side plane and other complex growth, as can be seen in the examples in Fig. 7. It is noteworthy, however, that pristine bullet rosettes were occasionally observed to grow at temperatures above $-40°$C. Figure 14 shows some rare examples of pristine bullet rosettes that were observed in a wave cloud with a cloud top temperature of $-36°$C. The examples shown in Fig. 14 comprise all of the clear, in-focus images of pristine bullet rosettes that were observed in this wave cloud. In this case, no part of the cloud top was observed to be at
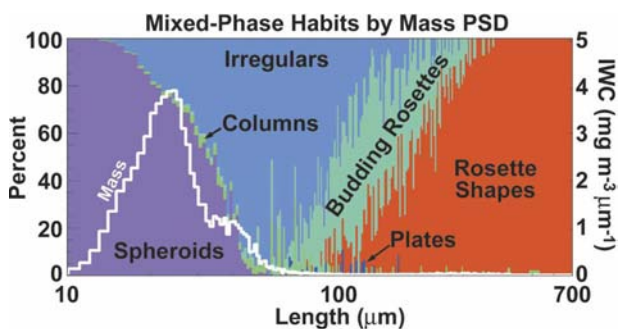

FIG. 13. Mass size distribution also showing the percentage of particle habits as a function of size for mixed-phase regions of all multiphase wave clouds.

---

[3] We refer to any crystal with spatial arms radiating from a central point as rosette shaped, or simply rosette. When the arms are each pristine columnar bullets, we refer to pristine bullet rosettes.
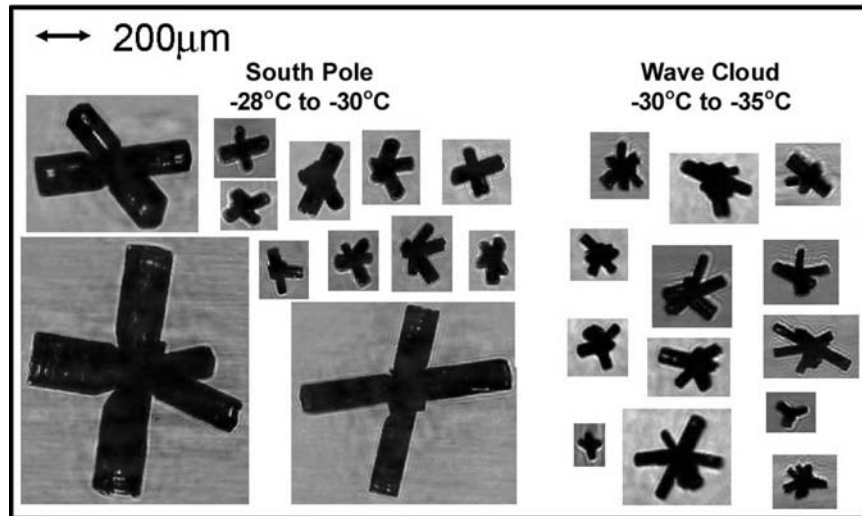
FIG. 14. Examples of pristine bullet rosettes imaged in a wave cloud, investigated 12 November 2002, and pristine bullet rosettes imaged at the surface that fell approximately 300 m from cirrus at the South Pole.

an altitude higher than the −36°C level. The Learjet crew observed that this cloud formed where there were no higher clouds and no other clouds for several hundred kilometers. The aircraft flew over cloud top at the beginning of the flight and detected no activity on any of the cloud particle probes. Next, it made horizontal penetrations of the cloud in 300-m vertical increments below cloud top, where the examples of pristine bullet rosettes shown in Fig. 14 were collected. At the end of the flight, the Learjet again measured a cloud top temperature of −36°C. Based on the visual observation that there were no higher clouds, along with the measurements in clear air over cloud top at the beginning and end of the flight, it is very unlikely that the crystals observed in Fig. 14 were nucleated at temperatures below −40°C.

Additional support that pristine bullet rosettes can nucleate and grow at temperatures above −40°C comes from CPI images collected at the South Pole, also shown in Fig. 14. In this case, the atmosphere was warmer than −33°C from the surface (700 mb) to 500 mb and no clouds above 600 mb were detected by a ground-based lidar and human observers. In this case, there were several more examples of pristine bullet rosettes than shown here, but the predominate crystal type was the more complex, not pristine, rosette shape.

The trends and exceptions observed in these wave clouds suggest that crystal habits grown under laboratory conditions (i.e., Bailey and Hallett 2004a,b; Bacon et al. 2003) are generally, but not strictly, applicable in natural clouds. One possible source for the difference is that, in the experiments described by Bailey and Hallett

(2004a), crystals nucleated on a nonice substrate while it is thought that, in natural clouds, bullet rosettes grow from the polycrystalline structure of a frozen drop (Pruppacher and Klett 1997). Solution drops, that is, wetted aerosols or very small drops less than 1 μm in diameter that have relatively high concentrations of dissolved salt, have been observed to freeze and produce rosette-shaped crystals in a cloud chamber (P. J. DeMott 2003, personal communication). This could be occurring in the colder regions of the wave clouds. In other laboratory experiments, Bacon et al. (2003) found that the substrate, in this case either frost or frozen drops, was critical to the morphology of the resulting crystal growth. They also found that, at the low supersaturations of that study and with crystals growing on ice substrates, traditional habits with temperature and supersaturation relationships were not followed. Where the more recent laboratory experiments (Bailey and Hallett 2004a,b; Bacon et al. 2003) differ from traditional results (e.g., Magono and Lee 1966), the recent results are more consistent with observations of natural clouds.

Rosettes shapes that are <200 μm and whose branches are not yet very long have been separated into another category, called budding rosettes. Examples of budding rosettes are also shown in the top half of Fig. 7. The remaining crystal habit categories included in Fig. 12 are plates, small irregulars, and large irregulars. Plates are rare in the wave cloud dataset. The break between the large and small irregulars was arbitrarily chosen at 200-μm length.
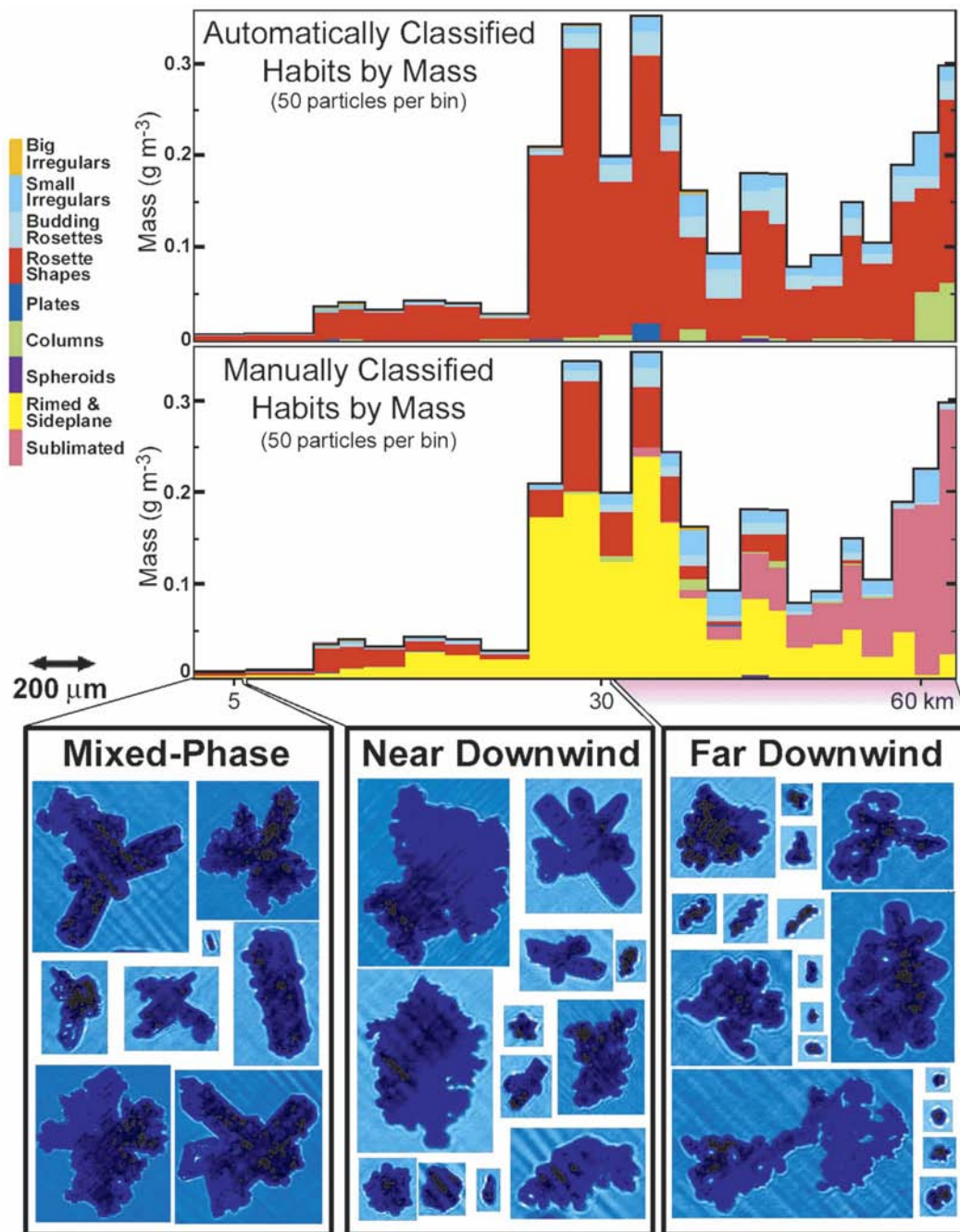
Figure 15 shows an evolution of particle images pro-

FIG. 15. Time series of mass content and mass-weighted habit percentages, both automatically and manually classified, of crystals larger than 50 μm. The cloud penetration was made at $-28°$C in the same cloud as shown in Figs. 6 and 7. Examples are shown of typical CPI images, including spatially complex rosette-shaped and sublimating crystals, observed in the three regions of multiphase wave clouds defined in Fig. 6.

ceeding downwind from the region with SLW to the downwind edge of cloud at $-28°$C on 20 October 2001. This is the same cloud shown in Figs. 6 and 7. The rosette-shaped crystals become more complex the farther downwind in the cloud observations are made.

This is understandable, since in addition to riming and side-plane growth, a variety of super- and subsaturation environments are experienced by the crystals as they progress through the cloud.

Manual classification of the particles was performed

for these data as well as the automatic classification that was applied to all the data. The example shown in Fig. 15 is typical of particle characteristics in multiphase wave clouds at temperatures above −37°C. Immediately downwind of the SLW is a region of mixed phase with mostly (80% by mass) unrimed and lightly rimed rosette shapes, with only a few columns and virtually no plates. Because of the relatively high LWC often found in the mixed-phase region, some particles are heavily rimed and, on rare occasions, small graupel particles are observed. Particle characteristics in the near-downwind region are similar to those of the mixed-phase region, with a gradual transition to characteristics observed in the far-downwind region. The underlying structure of the more complex crystals can often be seen clearly enough to identify the original crystal habit, of which the large majority are rosette shaped. The underlying crystal habit of particles in the far downwind can rarely be identified, often displaying intricate shapes with tenuous bridges, typical of particles that have experienced sublimation (Korolev and Isaac 2004). The automatic habit identification generally classified these particles as rosette shapes or large irregulars. The Learjet did not always exit the cloud on the eastern edge; however, on all cloud passes, particles in the extreme (greater than approximately 100 km) downwind region appeared to be sublimated and were generally smaller in size than in regions farther upwind.

At temperatures lower than approximately −37°C, in both the multiphase and all-ice clouds, budding rosettes (i.e., rosette shapes with short branches), a few pristine bullet rosettes, rosette shapes, and small columns, along with blocky irregulars and high number concentrations of small particles are generally observed. CPI observations suggest that most of the small (<50 μm) frozen ice particles in this region are not spherical but, instead, typically have a quasi-spheroidal shape (see Fig. 7), which may be multifaced "droxtals." As explained by Ohtake (1970), if crystals form from supercooled water droplets near −40°C, the droplets may freeze so quickly that the crystals do not have time to reach an equilibrium state for the development of normal hexagonal and rectangular faces. The result is a particle that appears to be quasi-spheroidal or potato shaped because the resolution of the image is not good enough to see the multiple facets. The region from −50° to −60°C is generally dominated by small quasi-spheroidal particles with budding rosettes and blocky irregulars. Between −55° and −60°C the particles are almost entirely small quasi-spheroidal particles. It should be noted that the optical properties of quasi-spheroidal particles (i.e., droxtals) and spherical par-

ticles may be quite different, particularly at short wavelengths (Mishchenko et al. 1996).

5. Wave clouds as a natural laboratory, the onset of riming, and side-plane growth

a. Background and analysis technique

There are a few studies reported in the literature of the riming threshold size of columnar crystals. Schlamp et al. (1975) made numerical simulations of riming on columnar crystals and found that riming should not be very sensitive to the length of the column and that the width[4] of the column should play the significant role. Their simulations showed that riming should start when the column width reaches about 50 μm. This has been supported by previous field studies where the ice crystals were collected on glass slides (Ono 1969; Zikmunda and Vali 1972). The observations also supported the theoretical prediction that riming occurred over the entire length of the columns.

Reports of studies of side-plane growth are scarce in the literature. Although side planes are often mentioned in the literature and have been observed in nearly all types of supercooled clouds, (e.g., Magono and Lee 1966; Mitchell 1996; Heymsfield and Miloshevich 2003), there has been little work that has shed light on how side planes originate and grow. There have been no reports in the literature of riming thresholds or observations of side plane using conventional (i.e., Knollenberg 1981) airborne optical probes because these probes are not capable of resolving individual drops and side plane on ice crystals. Replicators have much better resolution, but crystals larger than about 200 μm shatter on impact (Arnott et al. 1994), so interpretation of the images is often ambiguous. The CPI makes it possible to identify riming and side plane on ice crystals that are imaged on the fly as they pass through the instrument.

A study of the onset of riming and side-plane growth on columns and rosettes shapes was conducted by visually examining more than 75 000 ice crystal images from five wave clouds that contained SLW. Out of this total, 1568 crystals were selected on the basis of being able to identify crystal type, degree of riming, and side-plane growth. Figure 16 shows examples of crystals and the categories into which they were segregated. Once a crystal is heavily rimed, determination of the original crystal habit is highly subjective. To avoid this subjec-

---

[4] When referring to columns in this section, length refers to the standard geometrical length of a hexagonal column and width refers to the standard geometrical width.
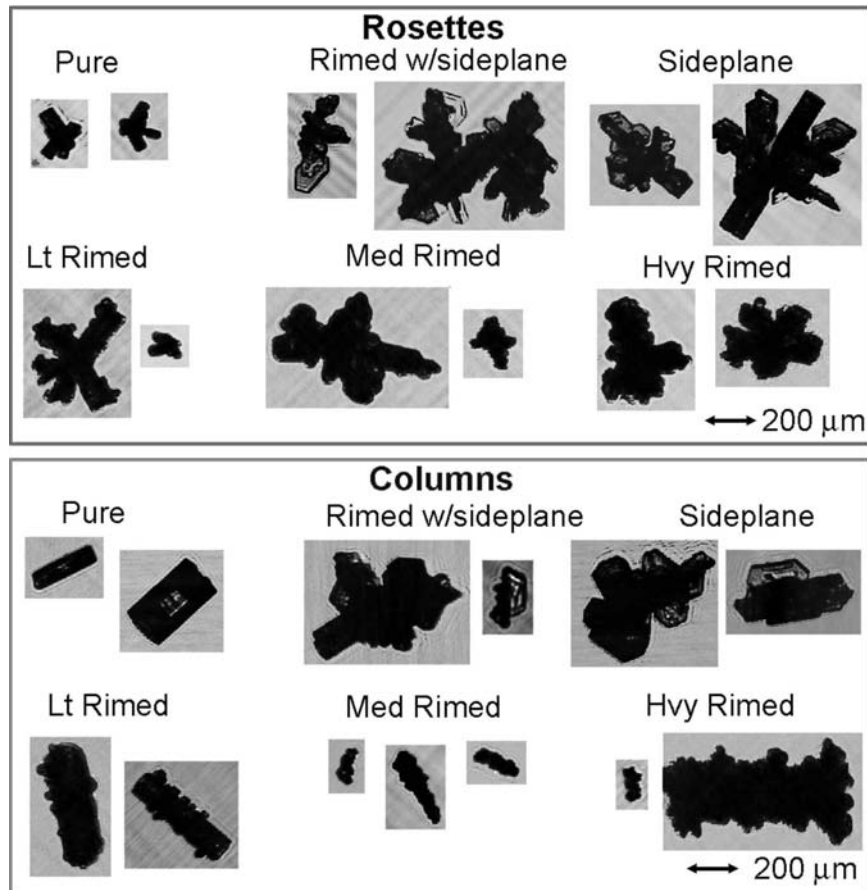
FIG. 16. Examples of ice crystals in wave clouds that were classified manually for use in the analysis of riming and side-plane characteristics.

tivity, only crystals whose original habits could be identified were used in this study. In addition, the crystals were categorized as to the location in the wave cloud at which they were observed, that is, mixed phase, near downwind, and far downwind (Fig. 6).

The riming onset results presented here for columns are consistent with the previous results of Ono (1969), provided only data from certain mixed-phase regions of cloud are used. If data from glaciated regions are included, then the consistent results are lost. This is because ice will continue to grow in the glaciated region of cloud as long as there is upward moving air. Similarly, if mixed-phase regions of jumbled clouds (clouds with multiple mixed-phase regions, see section 4b) are included, then the consistent results are again lost. It is possible that particles may grow larger than the threshold size for riming in regions without enough droplets for riming to occur and then fall or be advected into a mixed-phase region where they are observed. Thus, consistency with Ono's results was used as a test of whether a selected wave cloud makes a good natural laboratory for riming onset studies. It was found that

the clouds with a single mixed-phase region satisfied the test, while the jumbled clouds did not. Once this was established, riming onset was studied for rosette-shaped crystals, which has not previously been reported.

b. Results for columns

Ono (1969) presents results on the onset of riming with size of columnar ice crystals in warm (tops $-6°$ and $-5°C$, observations at $-2°C$) cumulus and stratocumulus clouds. Our results in wave clouds are similar. Figure 17 shows a transition from pristine to rimed columns at widths between 56 and 81 μm, consistent with Ono's result of 50–90 μm, since his study involved a greater number of crystals. Also consistent with Ono's results is the finding that column width is a better predictor of the onset of riming than length. Using length, the transition zone is much larger: from 117 to 312 μm. Column width is also a better predictor of riming onset than particle area (Fig. 18); area, however, is better than length. Using the square root of area, the transition occurs between 73 and 133 μm.
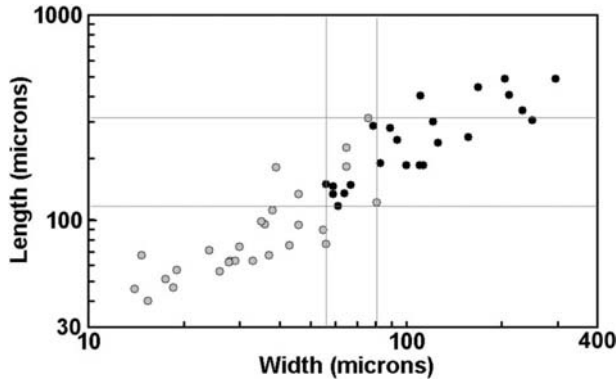
FIG. 17. Scatterplot of length vs width with pristine columns as shaded circles and crystals that are rimed as solid disks.

FIG. 19. Scatterplot of column length vs column width for all the pristine columns. Dotted lines represent aspect rations of 4 and 1, while the solid line represents an aspect ratio of 2.

The physical process of riming should not be very different in wave clouds than in cumulus and stratocumulus, and no difference has been found in this study. However, some other aspects of Ono's results in cumulus and stratocumulus do differ from our results in wave clouds. For example, Ono found that for warm and cold ($-32°$C stratus) columns, both crystal axes continue to grow until the minor axis (width in this study) reaches about 90 μm, after which growth is confined to the major axis. As a result of this, the aspect ratios of his columns vary considerably, and no column has a width much greater than 90 μm. For the columns shown in Fig. 17, the aspect ratio of the crystals is scattered around 2 and the widths exceed 90 μm. This difference from Ono's results is emphasized further in Fig. 19, which shows all the pristine columns regardless of location in cloud, instead of all the columns in only the mixed-phase regions (Fig. 17). The aspect ratios are still scattered around a value of about 2: crystal widths greatly exceed 90 μm and do not seem to be naturally

limited at any value. This is consistent with the laboratory results of Bailey and Hallett (2004a,b) for columnar crystals warmer than about $-35°$C.

c. Results for rosette shapes

Excellent agreement was found between Ono's (1969) results for the onset of riming of columns in cumulus and stratocumulus at $-5°$ to $-6°$C and our airborne CPI results in wave clouds. This builds confidence in the airborne CPI technique and allows us to expand the analysis to rosette-shaped ice crystals. Since rosette shapes are common in wave clouds and columns are rare, the dataset for studying rosette shapes is much larger (432 rosette-shaped crystals in the mixed-phase regions of the well-behaved wave clouds versus 51 columns).

For rosette-shaped crystals there is also a threshold size range for which riming begins. However, of the three size parameters—length, width, and area—none stand out as the dominant controlling factor, as width does for columns. This is understandable since the width of the arms is not represented by the width of the rosette crystal and because rosette crystals do not orient themselves horizontally, as is the tendency of falling columns. Results for length are shown in Fig. 20 since length is the most common parameter used to describe cloud particles. The smallest rimed rosette-shaped crystal is about 100 μm and almost all rosette-shaped crystals are rimed by about 300 μm.

d. Results for side planes

For both columns and rosette-shaped crystals, side planes were observed on crystals that were also rimed or, if rime was not apparent, the particle was already
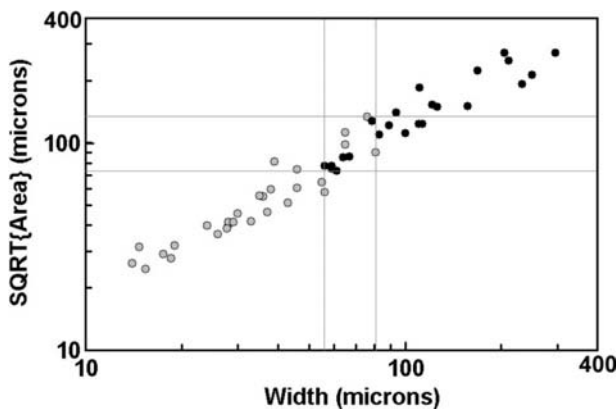

FIG. 18. Scatterplot of the square root of particle area vs width with pristine crystals as shaded circles and crystals that are rimed as solid disks.
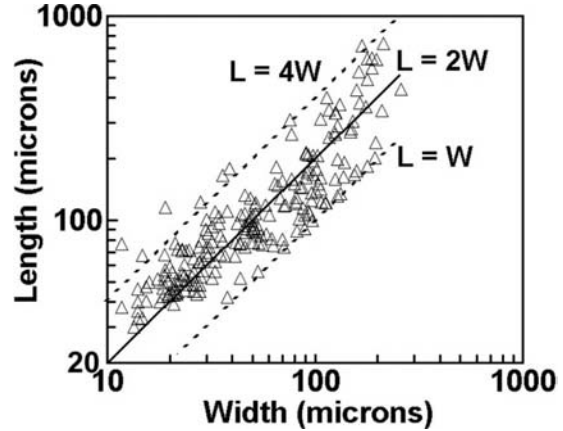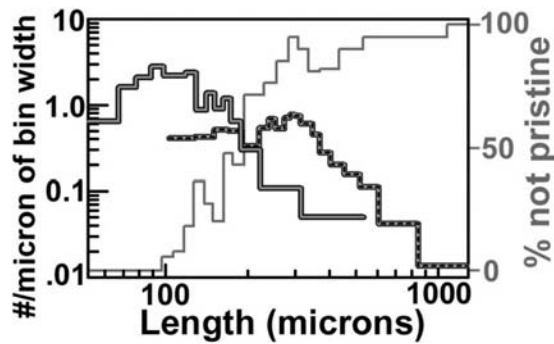
F_IG. 20. Relative PSDs using particle length for size, pristine rosettes: thick gray; rosettes rimed and/or with side planes: thick gray with black dashes; and percent rimed and/or with side planes: thin gray.

larger than the threshold size for riming to occur. This result suggests that side planes are continued growth by vapor deposition on rimed particles. M. Bailey (2004, personal communication) finds side-plane growth on rosettes in the laboratory, but only originating from the rosette center. Since there was no riming in Bailey's experiments, our observation that side-plane growth may only occur at a riming site is consistent with Bailey's laboratory observation that side-plane growth only occurs at the center of the rosette. In both cases, the sites of side-plane growth are locations of higher than normal stresses and, thus, defects and dislocations, which are sites where depositional growth tends to occur. In another laboratory study, Bacon et al. (2003) found that, at low supersaturations, side planes grew from frozen drop substrates but not from frost substrates, and conclude that defects and dislocations are key.

With regard to the crystallographic orientation of side-plane growth, Ono (1969) reports, "From an examination of some 200 crystals we conclude that, almost without exception, droplets accreted on the prism faces between −15° and −20°C take the same orientation as the substrate." In the wave cloud dataset, which was collected at lower temperatures (−28° to −37°C) than Ono's data, there is no apparent preferred crystallographic orientation of side planes relative to the substrate's crystallographic orientation and, if there is a preferred orientation, the images suggest that it is perpendicular to the substrate's orientation (Fig. 16). The ambiguity is due to the fact that, even with high resolution, it is difficult to determine full three-dimensional information from two-dimensional images. The relatively lower temperatures of the wave cloud dataset may cause the difference in observed orientation of the side planes. For example, the greater fraction of the droplet that freezes upon initial contact with the sub-

strate, as well as the more rapid subsequent freezing of the remainder of the droplet at lower temperatures, might explain the random orientation.

6. Area–length parameterizations

Parameterized relationships between particle projected area (A) and length (L) are useful in radiation studies, especially retrievals from remote sensors and modeling studies. This section presents A versus L parameterizations based on least squares regression of CPI image data collected in wave clouds. Lawson et al. (2006b, hereafter Part II) report A versus L parameterizations for CPI image data collected in cirrus clouds. The regression is found for the logarithms of A and L, so the parameterization is of the form:

$$A = \alpha L^{\beta}. \qquad (1)$$

The wave cloud data are segregated according to temperature and certain crystal types: rosettes, irregulars, and columns. Rosettes and irregulars are included because they are the dominant crystal types in wave clouds, and in cirrus (Part II). Columns are included, even though they are a minority constituent, because they do exist in greater numbers in other clouds. Table 4 displays the results for particles >50 μm, which is analogous to the "large mode" of the PSD in cirrus as defined by Ivanova et al. (2001). The small mode can be parameterized independently assuming the particles are spherical.

For self-similar crystals, that is, crystals that retain the same geometrical shape as they grow, $\beta = 2$. For the extreme case of a column that grows in length but not width, β will equal 1, which is the result Ono found for columns once the width reaches 90 μm (see section 5 above). The crystals in the wave cloud dataset (and the cirrus dataset in Part II) tend to grow faster in length than width and thus have values of β between 1 and 2. The smaller the β, the more elongated the crystal or crystal elements are becoming as they grow. A clear trend is seen in Table 4 for β values to decrease with decreasing temperature. That is, the colder the crystal, the more elongated it becomes as it grows. The "all columns between −37° and −30°C" group seems to be anomalous and contradict this trend, but that is explained by inspection of the uncertainty in β ($\Delta\beta$), determined by a bootstrap method (Efron and Tibshirani 1994). The uncertainty in β is very high for that group. Also apparent in Table 4 is the tendency for particles in the mixed-phase regions to become elongated with growth at a slower rate than the other crystals. That is, β is larger for the same crystal type in the mixed-phase region than it is in the glaciated regions.

TABLE 4. The results of fitting Eq. (1) to various subsets of CPI images >50 μm collected in wave clouds. Segregation is according to three crystal types: rosettes, irregulars, and columns. Further segregation restricts each of these to temperature ranges and to the subset found in mixed-phased (MP) cloud only. A subset of the complex rosette-shaped crystals was additionally segregated according to degree of riming. In addition to the Eq. (1), parameters α and β, an uncertainty in β ($\Delta\beta$), estimated by a bootstrap technique, and the number of crystals in that category (N) are shown.

Segregation criterion (°C)	α	β	$\Delta\beta$	N
All rosettes $-60 \leq T < -37$	2.3507	1.6591	0.0170	1217
All rosettes $-37 \leq T < -30$	1.2867	1.7964	0.0069	2380
All rosettes $-30 \leq T \leq -20$	0.8085	1.8795	0.0082	1601
MP rosettes $-35 \leq T < -30$	0.8264	1.8852	0.0164	152
MP rosettes $-30 \leq T \leq -20$	0.7297	1.8993	0.0197	304
All irregulars $-60 \leq T < -37$	2.3400	1.6664	0.0084	5121
All irregulars $-37 \leq T < -30$	1.4986	1.7807	0.0042	7256
All irregulars $-30 \leq T \leq -20$	1.0427	1.8475	0.0063	1838
MP irregulars $-35 \leq T < -30$	1.4294	1.7913	0.0231	390
MP irregulars $-30 \leq T \leq -20$	0.9590	1.8661	0.0109	594
All columns $-60 \leq T < -37$	0.9360	1.8111	0.0366	273
All columns $-37 \leq T < -30$	1.7765	1.6402	0.1426	96
All columns $-30 \leq T \leq -20$	0.4636	1.9493	0.0182	190
MP columns $-35 \leq T < -30$	0.2136	2.0897	0.4496	7
MP columns $-30 \leq T \leq -20$	0.3475	2.0186	0.0425	24
Heavily rimed rosette shaped	0.6843	1.9163	0.0158	494
Medium-rimed rosette shaped	0.9561	1.8511	0.0172	451
Lightly rimed rosette shaped	1.1344	1.8156	0.0143	527

FIG. 21. Plots of particle area vs length for irregulars and rosettes >50 μm for three temperature regions in wave clouds. Also shown are the best-fit power-law equations and the number of particles (N) in each dataset. Note that there are actually more particles in the irregular category, but they are tightly contained in lengths less than approximately 600 μm.

The $A(L)$ relationships for rosettes and irregulars are nearly the same within each temperature regime and, since these particles dominate wave clouds, a single $A(L, T)$ function could be used to represent all wave cloud particles. Figure 21 shows plots of $A(L)$ relationships for rosettes and irregulars. Fortuitously, and apparently coincidentally, the similarity in the $A(L)$ relationships for rosettes and irregulars could greatly facilitate parameterizations of radiative transfer in remote retrievals and modeling studies of wave clouds.

It is worth mentioning that the statement in section 4c, that the colder clouds tend to have a greater percentage of small spheroidal particles than the warmer regions, is not contradictory to the data presented in this section. Here, results pertain to the elongation of particles >50 μm as they grow, while the statement in section 4c pertains to the percentage of particles <50 μm. In the colder regions the few particles that do grow to sizes >50 μm experience a greater degree of elongation than similar sized particles at higher temperatures.

The "all rosette shapes" categories contain all the particles automatically classified as rosette shaped for each included pe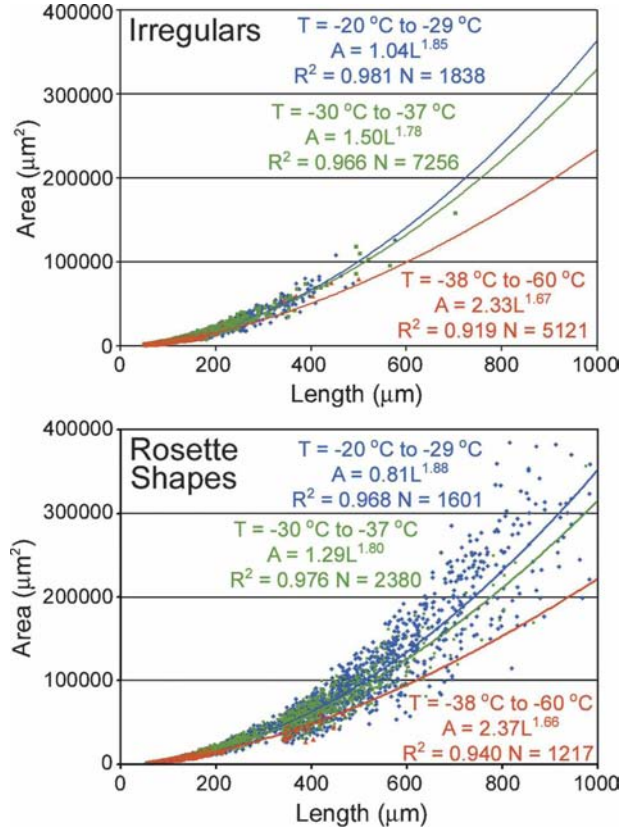netration. Penetrations for which the automatic classification of rosette shapes was poor were not included. As discussed in section 4g above, most particles automatically classified as rosette shapes are not pristine and generally have side-plane, rime, or other complex structure. A subset of these rosette-shaped particles was manually classified as to their degree of riming and the same $A(L)$ analysis applied. These results are in the last three rows of Table 4 and, as expected, the more heavily rimed particles were less elongated as they grew.

7. Summary and discussion

Microphysical data from 133 Learjet research aircraft penetrations of 17 wave clouds are presented. For five generalized wave cloud regions the mean and standard deviations of bulk microphysical parameters, crystal habit percentages, and particle size distributions are presented. In addition, time series of 11 different individual penetrations are shown. They were chosen to

demonstrate both general trends observed in the wave cloud dataset and exceptions to those trends.

Most aspects of the wave cloud observations are interpreted and understandable in terms of textbook cloud physics. However, a few aspects of the observations cannot be so easily explained. In some cases hypotheses have been put forward as tentative explanations. In particular, the lack of correlation of ice concentration with temperature may be due to the temperature effect being less strong than other influences that were not measured, such as variations in aerosol populations and vertical velocities. The sudden increase in ice concentration at the glaciation transition point may be due to a recently discovered phenomenon: that contact nucleation is effective from inside droplets as well as via dry particles making contact from outside droplets (Shaw et al. 2005; Durant and Shaw 2005). The commonly observed additional structure of the wave clouds over that of simple gravity waves is presented, but speculation as to its cause is beyond the scope of this work. The extensive regions of SLW that are consistently observed near the leading edges of wave clouds suggest that deposition nucleation is insignificant at temperatures higher than $-37°$C. Otherwise, ice would be observed much sooner in the SLW regions.

Particle size distributions in the mixed-phase and all-ice regions warmer than $-37°$C displayed a notable bimodal distribution. The small mode in the all-ice region appears to be the result of freezing of supercooled cloud drops very near the downwind end of the mixed-phase region. The large mode appears to be the result of ice particles nucleated earlier in the mixed-phase region that subsequently grew rapidly via the Bergeron–Findeison process, riming, and aggregation. Bimodal size distributions were not characteristic of regions of wave clouds colder than $-38°$C.

Crystal habits of ice particles >50 μm were determined. Columns accounted for $<1\%$ of the ice mass of particles >50 μm and plates were virtually nonexistent. Small spheroidal and irregular-shaped particles dominate the number concentration when all particle sizes are included. Rimed ice particles and particles with side planes were observed in the mixed phase and downwind of the mixed-phase region at $T \geq -37°$C. In the far-downwind region the particles appear to be sublimated with rounded edges, often with tenuous bridges and intricate curves, similar to sublimating particles observed by Korolev and Isaac (2004). At $T < -38°$C, the particles are noticeably smaller, the particle concentrations are lower, and the shapes are mostly spheroidal, irregular, and small rosette shapes. At $T < -55°$C the particles are almost always small (<50 μm) and have mostly spheroidal shapes. Polycrystals with rosette shapes are the predominant recognizable particle habit and occur within a temperature range from about $-55°$ to $-25°$C. The characteristics of polycrystalline rosette shapes generally followed the laboratory findings of Bailey and Hallett (2004a). That is, pristine bullet rosettes are almost never found at temperatures $>-40°$C. Instead, rosette shapes with more complex features, including side-plane and irregular growth shapes, are found at temperatures from about $-40°$ to $-25°$C. However, this dataset contains a few exceptions to their strict observation that pristine bullet rosettes are not found at temperatures $>-40°$C.

Despite the complexity generally found in wave clouds, select wave clouds can still be found that are consistent enough to be used as natural laboratories for cloud physics research. A study of the riming threshold size of columns in wave clouds is in good agreement with the results of Ono (1969), showing that a column width from about 50 to 90 μm is the best predictor of riming size threshold. The first reported studies of the riming threshold size of rosette-shaped crystals showed that the smallest rimed rosette is about 100 μm in length while most rosette shapes are rimed by about 300 μm. The threshold size for side-plane growth is very consistent with the respective riming threshold sizes of columns and rosette shapes, suggesting that side-plane growth occurs at a riming site.

REFERENCES

Arnott, W. P., Y. Dong, and J. Hallett, 1994: Role of small ice crystals in radiative properties of cirrus: A case study, FIRE II, November 22, 1991. *J. Geophys. Res.,* **99,** 1371–1381.

Bacon, N. J., M. B. Baker, and B. D. Swanson, 2003: Initial stages in the morphological evolution of vapour-grown ice crystals: A laboratory investigation. *Quart. J. Roy. Meteor. Soc.,* **129,** 1903–1927.

Bailey, M., and J. Hallett, 2004a: Growth rates and habits of ice crystals between $-20°$ and $-70°$C. *J. Atmos. Sci.,* **61,** 514–544.

——, and ——, 2004b: A new habit diagram and mass parameters for atmospheric ice crystals from $-20°$C to $-70°$C. *Proc. 14th Int. Conf. on Clouds and Precipitation,* Vol. 1, Bologne, Italy, International Commission of Clouds and Precipitation, 703–706.

Baker, B. A., and R. P. Lawson, 2006: Improvement in determination of ice water content from two-dimensional particle imagery. Part I: Image-to-mass relationships. *J. Appl. Meteor. Climatol.,* **45,** 1282–1290.

Baumgardner, D., and A. Korolev, 1997: Airspeed corrections for optical array probe sample volumes. *J. Atmos. Oceanic Technol.,* **14,** 1224–1229.

——, W. A. Cooper, and J. E. Dye, 1990: Optical and electronic limitations of the forward-scattering spectrometer probe. *Liquid Particle Size Measurements Techniques,* ASTM Special Tech. Publ. 1083, Vol. 2, American Society for Testing and Materials, 115–127.

Beard, K. V., 1992: Ice initiation in warm-base convective clouds: An assessment of microphysical mechanisms. *J. Atmos. Res.,* **28,** 125–152.

Brenguier, J.-L., 1989: Coincidence and dead-time corrections for particle counters. Part II: High concentration measurements with an FSSP. *J. Atmos. Oceanic Technol.,* **6,** 585–598.

Cober, S. G., G. A. Isaac, and A. V. Korolev, 2001: Assessing the Rosemount icing detector with in situ measurements. *J. Atmos. Oceanic Technol.,* **18,** 515–528.

Cooper, W. A., 1988: Effects of coincidence on measurements with a forward scattering spectrometer probe. *J. Atmos. Oceanic Technol.,* **5,** 823–832.

——, 1995: Ice formations in wave clouds: Observed enhancement during evaporation. Preprints, *Conf. on Cloud Physics,* Dallas, TX, Amer. Meteor. Soc., 147–152.

Durant, A. J., and R. A. Shaw, 2005: Evaporation freezing by contact nucleation inside-out. *Geophys. Res. Lett.,* **32,** L20814, doi:10.1029/2005GL024175.

Efron, B., and R. J. Tibshirani, 1994: *An Introduction to the Bootstrap.* Chapman and Hall, 436 pp.

Field, P. R., and Coauthors, 2001: Ice nucleation in orographic wave clouds: Measurements made during INTACC. *Quart. J. Roy. Meteor. Soc.,* **127,** 1493–1512.

Gayet, J., G. Febvre, and H. Larsen, 1996: The reliability of the PMS FSSP in the presence of small ice crystals. *J. Atmos. Oceanic Technol.,* **13,** 1300–1310.

Hallett, J., 1968: Nucleation and growth of ice crystals in water and biological systems. *Low Temperature Biology of Foodstuffs,* J. Hawthorne, Ed., Pergamon Press, 23–52.

Heymsfield, A. J., and L. M. Miloshevich, 1993: Homogeneous ice nucleation and supercooled liquid water in orographic wave clouds. *J. Atmos. Sci.,* **50,** 2335–2353.

——, and ——, 1995: Relative humidity and temperature influences on cirrus formation and evolution: Observations from wave clouds and FIRE II. *J. Atmos. Sci.,* **52,** 4302–4326.

——, and ——, 2003: Parameterizations for the cross-sectional area and extinction of cirrus and stratiform ice cloud particles. *J. Atmos. Sci.,* **60,** 936–956.

Ivanova, D., D. L. Mitchell, W. P. Arnott, and M. Poellot, 2001: A GCM parameterization for bimodal size spectra and ice mass removal rates in mid-latitude cirrus clouds. *J. Atmos. Res.,* **59-60,** 89–113.

Knollenberg, R. G., 1981: Techniques for probing cloud microstructure. *Clouds Their Formation, Optical Properties, and Effects,* P. V. Hobbs and A. Deepak, Eds., Academic Press, 15–91.

Korolev, A. V., and G. A. Isaac, 2004: Observation of sublimating ice crystals in clouds. *Proc. 14th Int. Conf. on Clouds and Precipitation,* Vol. 2, Bologne, Italy, International Commission of Clouds and Precipitation, 808–811.

——, J. W. Strapp, G. A. Isaac, and A. N. Nevzorov, 1998: The Nevzorov airborne hot-wire LWC-TWC probe: Principle of operation and performance characteristics. *J. Atmos. Oceanic Technol.,* **15,** 1495–1510.

Lawson, R. P., B. A. Baker, C. G. Schmitt, and T. L. Jensen, 2001: An overview of microphysical properties of Arctic clouds observed in May and July during FIRE ACE. *J. Geophys. Res.,* **106,** 14 989–15 014.

——, D. O'Connor, P. Zmarzly, K. Weaver, B. A. Baker, Q. Mo, and H. Jonsson, 2006a: The 2D-S (stereo) probe: Design and preliminary tests of a new airborne, high-speed, high-resolution particle imaging probe. *J. Atmos. Oceanic Technol.,* **23,** 1462–1477.

——, B. A. Baker, B. Pilson, and Q. Mo, 2006b: In situ observations of the microphysical properties of wave, cirrus and anvil clouds. Part II: Cirrus clouds. *J. Atmos. Sci.,* **63,** 3186–3203.

Magono, C., and C. W. Lee, 1966: Meteorological classification of natural snow crystals. *J. Fac. Sci., Hokkaido Univ.,* **7,** 320–355.

Matrosov, S. Y., 1993: Possibilities of cirrus particle sizing from dual-frequency radar measurements. *J. Geophys. Res.,* **98,** 20 675–20 683.

——, 1997: Variability of microphysical parameters in high-altitude ice clouds: Results of the remote sensing method. *J. Appl. Meteor.,* **36,** 633–648.

Mazin, I. P., A. V. Korolev, A. Heymsfield, G. A. Isaac, and S. G. Cober, 2001: Thermodynamics of icing cylinder for measurements of liquid water content in supercooled clouds. *J. Atmos. Oceanic Technol.,* **18,** 529–542.

Mishchenko, M. I., W. B. Rossow, A. Macke, and A. A. Lacis, 1996: Sensitivity of cirrus cloud albedo, bidirectional reflectance, and optical thickness retrieval accuracy to ice-particle shape. *J. Geophys. Res.,* **101,** 16 973–16 985.

Mitchell, D. L., 1996: Use of mass and area-dimensional power laws for determining precipitation particle terminal velocities. *J. Atmos. Sci.,* **53,** 1710–1723.

——, R. Zhang, and R. L. Pitter, 1990: Mass-dimensional relationships for ice particles and the influence of riming on snowfall rates. *J. Appl. Meteor.,* **29,** 153–163.

Ohtake, T., 1970: Unusual crystal in ice fog. *J. Atmos. Sci.,* **27,** 509–511.

Ono, A., 1969: The shape and riming properties of ice crystals in natural clouds. *J. Atmos. Sci.,* **26,** 138–147.

Pruppacher, H. R., and J. D. Klett, 1997: *Microphysics of Clouds and Precipitation.* Kluwer Academic, 954 pp.

Rangno, A. L., and P. V. Hobbs, 1983: Production of ice particles in clouds due to aircraft penetrations. *J. Climate Appl. Meteor.,* **22,** 214–232.

Schlamp, R. J., H. R. Purppacher, and A. E. Hamielec, 1975: A numerical investigation of the efficiency with which simple columnar ice crystals collide with supercooled water drops. *J. Atmos. Sci.,* **32,** 2330–2337.

Shaw, R. A., and D. Lamb, 1999: Experimental determination of the thermal accommodation and condensation coefficients of liquid water. *J. Chem. Phys.,* **111,** 10 659–10 663.

——, A. J. Durant, and Y. Mi, 2005: Heterogeneous surface crystallization observed in undercooled water. *J. Phys. Chem.,* **109B,** 9865–9868.

Strapp, J., W. F. Albers, A. Reuter, A. V. Korolev, U. Maixner, E. Rashke, and Z. Vukovic, 2001: Laboratory measurements of the response of a PMS OAP-2DC. *J. Atmos. Oceanic Technol.,* **18,** 1150-1170.

Young, K. C., 1973: The role of contact nucleation in ice initiation in clouds. *J. Atmos. Sci.,* **31,** 768–776.

Zikmunda, J., and B. Vali, 1972: Fall patterns and fall velocities of rimed ice crystals. *J. Atmos. Sci.,* **29,** 1334–1347.